

12-15-2012

## Experimental Characterization and Modeling of the Brittle and Ductile Failure of Polypropylene and Copolymer Polypropylene

Brian Edward Denton

Follow this and additional works at: <https://scholarsjunction.msstate.edu/td>

---

### Recommended Citation

Denton, Brian Edward, "Experimental Characterization and Modeling of the Brittle and Ductile Failure of Polypropylene and Copolymer Polypropylene" (2012). *Theses and Dissertations*. 2138.  
<https://scholarsjunction.msstate.edu/td/2138>

This Graduate Thesis - Open Access is brought to you for free and open access by the Theses and Dissertations at Scholars Junction. It has been accepted for inclusion in Theses and Dissertations by an authorized administrator of Scholars Junction. For more information, please contact [scholcomm@msstate.libanswers.com](mailto:scholcomm@msstate.libanswers.com).

Experimental characterization and modeling of the brittle and ductile failure of  
polypropylene and copolymer polypropylene

By

Brian Edward Denton

A Thesis  
Submitted to the Faculty of  
Mississippi State University  
in Partial Fulfillment of the Requirements  
for the Degree of Master of Science  
in Mechanical Engineering  
in the Department of Mechanical Engineering

Mississippi State, Mississippi

December 2012

Copyright by  
Brian Edward Denton  
2012

Experimental characterization and modeling of the brittle and ductile failure of  
polypropylene and copolymer polypropylene

By

Brian Edward Denton

Approved:

---

Jean-Luc Bouvard  
Assistant Research Professor of  
Mechanical Engineering  
(Director of Thesis)

---

Mark F. Horstemeyer  
Professor of Mechanical Engineering  
(Major Professor)

---

Hongjoo Rhee  
Assistant Research Professor  
(Committee Member)

---

Kalyan K. Srinivasan  
Assistant Professor of Mechanical  
Engineering  
(Graduate Coordinator)

---

Sara A. Rajala  
Dean of the Bagley College of  
Engineering



Name: Brian Edward Denton

Date of Degree: December 15, 2012

Institution: Mississippi State University

Major Field: Mechanical Engineering

Major Professor: Mark F. Horstemeyer

Director of Thesis: Jean-Luc Bouvard

Title of Study: Experimental characterization and modeling of the brittle and ductile failure of polypropylene and copolymer polypropylene

Pages in Study: 77

Candidate for Degree of Master of Science

Research areas within the automotive industry are dedicated to reducing the weight and emissions of vehicles. Through the application of lightweight materials, such as polymers, fuel consumption and production costs can be decreased. Therefore, understanding the mechanical responses and failure mechanisms of these materials is significant to the development and design of vehicular structural components. Experimental tests were performed to capture the time, temperature, and stress state dependence, as well as failure mechanisms and large-strain mechanical responses of polypropylene (PP) and copolymer polypropylene (co-PP). Alongside studying the mechanical responses of PP and co-PP, the deformation mechanisms associated with the ductile and brittle failures were also examined. By applying an Internal State Variable (ISV) model, the mechanical behavior of PP and co-PP under various strain rates and temperatures was predicted. Phenomenological, mechanics based failure criteria were also applied to the model to predict the ductile or brittle failure of the materials.

## ACKNOWLEDGEMENTS

I would like to express sincere gratefulness to the countless people without whose support this thesis could not have materialized. First of all, I would like to acknowledge both of my advisors: Dr. Mark Horstemeyer and Dr. Jean-Luc Bouvard. They have been patient with me through my graduate school career, and I am very thankful for their tireless efforts in guidance and assistance throughout this research.

Next, expressed appreciation is due for my other committee member, Dr. Hongjoo Rhee, for the invaluable aid and direction provided by him. I am especially grateful that I had the opportunity to work alongside Clemence Bouvard and for her countless hours of teaching me ABAQUS.

I would like to thank Mr. Jim Kolb, senior director of Automotive for the American Chemistry Council, for funding this study under Grant No. 011104-001. I would also like to thank Dr. Mike Wyzgoski, consultant for American Chemistry Council, for his guidance and his constant availability in this project. Thank you to ExxonMobil Chemical Company for providing the different thermoplastics investigated in this project and the Center for Advanced Vehicular Systems (CAVS) at Mississippi State University for its support.

## TABLE OF CONTENTS

ACKNOWLEDGEMENTS .....	v
LIST OF TABLES .....	viii
LIST OF FIGURES .....	ix
CHAPTER	
I. INTRODUCTION .....	1
II. EXPERIMENTAL METHODS AND RESULTS.....	5
2.1 Materials .....	5
2.2 Mechanical Testing .....	7
2.3 Results of Mechanical Testing.....	11
2.3.1 Compression .....	11
2.3.2 Tension.....	13
2.3.3 Impact .....	15
2.3.4 Three Point Bending .....	18
III. FRACTURE SURFACE MORPHOLOGY .....	21
3.1 Specimen Preparation .....	21
3.2 Polypropylene Deformation.....	21
3.2.1 Brittle Failure .....	21
3.2.2 Ductile Failure .....	26
3.3 Copolymer Polypropylene Deformation.....	28
3.3.1 Brittle Failure .....	28
3.3.2 Ductile Failure .....	29
3.3.3 Quantitative Microstructure Characterization.....	33
IV. NUMERICAL SIMULATIONS.....	36
4.1 Model for Thermoplastics.....	36
4.2 Finite Element Analysis Model .....	40
4.3 Model Results .....	46
4.3.1 Compression .....	46
4.3.2 Tension.....	47
4.3.3 Impact .....	48

4.3.4	Three Point Bending .....	50
V.	APPLICATION OF ACC FAILURE CRITERIA.....	54
5.1	Brittle Failure Criteria.....	54
5.2	Ductile Failure Criteria .....	58
VI.	SUMMARY .....	62
	REFERENCES .....	64
APPENDIX		
A.	INTERNAL STATE VARIABLE MODEL CALIBRATION.....	67
A.1	One Dimensional Model .....	68
A.2	Parameters Identification .....	69
B.	GEOMETRY AND BOUNDARY CONDITIONS OF NUMERICAL SIMULATIONS .....	73
B.1	Tensile Simulations.....	74
B.2	Impact Simulations .....	74
B.3	Three Point Bending Simulations .....	76

## LIST OF TABLES

2.1	Properties of Polypropylene and Copolymer Polypropylene [12-13].....	6
3.1	Microstructure Property Quantification of a Co-PP Tension Specimen at 25°C and 0.0005/s.....	34
3.2	Microstructure Property Quantification of a Co-PP Tension Specimen at -20°C and 0.01/s.....	34
3.3	Microstructure Property Quantification of a Co-PP Small Notch Thin Three Point Bending Specimen at 25°C and 0.1667 mm/s.....	35
4.1	Three dimensional model summary .....	37
4.2	Parameter identification for 3D model for PP and co-PP .....	39
A.1	One dimensional model summary .....	68

## LIST OF FIGURES

2.1	Spherulites in (a) PP and (b) impact PP copolymer [15] .....	7
2.2	Specimen geometry for tension tests (Type I) .....	8
2.3	Impact test set-up with specimen secured in the fixture .....	9
2.4	Three point bending specimen geometry and dimensions .....	10
2.5	Effect of temperature and strain rate on the large strain compressive behavior of PP compared to co-PP .....	12
2.6	Mechanisms associated with the plastic deformation of crystalline polymers explained on the example of isotactic PP: curve 1, channel die compression; curve 2, tensile experiment [16] .....	13
2.7	Stress-strain curves at different strain rates and temperatures for PP and co-PP .....	14
2.8	Effect of temperature and loading rate for impact tests on PP and co-PP .....	16
2.9	Curves of peak load versus displacement for impact tests on (a) PP and (b) co-PP .....	17
2.10	Curves of failure load versus displacement for three point bend tests for PP and co-PP .....	19
3.1	SEM images of PP virgin surface .....	22
3.2	Brittle failure of PP tension specimen at -20°C and 0.1/s .....	23
3.3	Brittle failure of PP tension specimen at 25°C and 0.1/s .....	24
3.4	Fracture surface of PP small notch thick three point bending specimen at 0.1667 mm/s and 25°C .....	25
3.5	Fracture surface of PP large notch thin three point bending specimen at 0.1667 mm/s and 25°C .....	26

3.6	Ductile features on a PP large notch thin specimen.....	27
3.7	Ductile features on the edge of a PP tension specimen tested at 25°C and 0.1/s .....	28
3.8	SEM images of co-PP virgin surface .....	29
3.9	Fracture surface of co-PP tension specimen at 25°C and 0.01/s .....	30
3.10	Ductile failure of a co-PP tension specimen at -20°C and 0.01/s .....	31
3.11	Small notch thick three-point bending test specimen for co-PP at 0.1667 mm/s and 25°C.....	32
3.12	Small notch thin three-point bending test specimen for co-PP at 0.1667 mm/s and 25°C.....	33
4.1	(a) Coarse mesh and (b) fine mesh at notch of three point bending model using C4D8R elements .....	41
4.2	Mesh refinement results of three point bending model (Polycarbonate).....	42
4.3	Three point bend mesh containing C3D10M (tetrahedral) elements.....	43
4.4	Three point bending model results comparing C4D8R (hex) elements and C3D10M (tet) elements.....	44
4.5	Effect of friction during impact simulations of PP at 30 mm/s and 25°C .....	45
4.6	Effect of friction during three point bending simulations of PP small notch thin specimens at 0.1667 mm/s and 25°C .....	46
4.7	Comparison of the ISV based model to the experimental data for uniaxial compression of PP and co-PP at different strain rates and temperatures.....	47
4.8	Comparison of the ISV model to the experimental data for uniaxial tension of PP at 0.1/s and co-PP at 0.01/s at different temperatures .....	48
4.9	Comparison of the ISV model to the experimental data for uniaxial tension of PP at 0.1/s and co-PP at 0.01/s at different temperatures .....	50
4.10	Comparison of the ISV model to the experimental data for three point bending of PP and co-PP on thin and thick specimens.....	51
4.11	Stress concentration at the notch on three point bending tests for PP .....	52

4.12	Stress concentration at the notch on three point bending tests for co-PP .....	53
5.1	Evolution of the maximum principal stress for three point bending regarding the different specimen thicknesses .....	55
5.2	Determination of maximum principal stress failure criterion for PP .....	56
5.3	Evolution of the maximum principal stress for impact tests at 3 mm/s at -20, 25, and 70°C .....	57
5.4	Ratio of critical maximum principal stress to yield stress as a function of strain rate for impact tests at different strain rates and temperatures .....	58
5.5	Determination of failure strain criterion for co-PP .....	59
5.6	Equivalent plastic failure strain as a function of strain rate for impact tests of PP and co-PP at different strain rates and temperatures .....	59
5.7	Ductile failure criterion applied to three point bending tests for co-PP thick specimens .....	60
A.1	Description of the different steps to fit the material parameters: (a) capturing the time dependence, (b) capturing the strain hardening, (c) capturing the nonlinear yield peak, and (d) capturing the unloading of the Bauschinger effect .....	71
B.1	Geometry, dimensions, and boundary conditions for tension simulations .....	74
B.2	Boundary conditions for axisymmetric impact simulations .....	75
B.3	Surface to surface contact used during impact simulations .....	75
B.4	Mesh of impact specimens used for simulations .....	76
B.5	Dimensions and boundary conditions of the three point bend model .....	77



## CHAPTER I

### INTRODUCTION

Uses for plastic materials have increased during the last couple of decades due to their remarkable balance of mechanical properties and low densities. In some industries, such as the automotive industry, the development and application of lightweight materials like polymers contribute to reductions in costs, such as savings in fuel consumption as well as reduced emissions and production costs. For this increase in new applications of polymeric materials, expensive mechanical testing must also be performed; however, high fidelity material models with finite element method-based engineering design tools can be used instead for predicting the structural performance of plastic components. When compared to metallic materials, plastic distinguishes itself as being highly temperature and loading rate sensitive, and exhibits special post yield behavior with strain softening and hardening. Therefore, through the use of constitutive models, conceptual designs can be assessed and optimized, thereby shortening the costly prototyping and testing cycles.

This work uses mechanical experiments to characterize the mechanical response of two thermoplastic materials: polypropylene (PP) and a copolymer polypropylene (co-PP). Polypropylene is a semi-crystalline polymer that has wide applications in the automotive industry; however, one disadvantage of PP is its low fracture toughness at low temperatures or under impact conditions. To improve the toughness and impact

resistance of PP, it can be modified or combined with particle fillers, such as rubbers, compatible with the homopolymer to create a copolymer polypropylene. The resulting material exhibits a much better fracture toughness and impact resistance. These material particles that are incorporated into the PP have a strong influence on the macroscopic behavior of the material by absorbing energy; thus, a good knowledge of the material under different stress states and strain rates and the microscopic mechanisms which lead to the macroscopic response and material failure are necessary. These mechanical tests are used to capture the time, temperature, and stress state dependence that thermoplastics exhibit.

Alongside studying the mechanical responses and failures of PP and co-PP, the deformation mechanisms associated with the brittle and ductile failures are also examined. Ductile failure is characterized by slow, stable crack growth as the material experiences significant plastic deformation before failure. Brittle failure is characterized by fast, unstable crack growth and is sudden and often without warning. Brittle failure requires no further energy to propagate once initiated. Materials experiencing lower temperatures, higher rates of loading, or containing more severe stress concentrations are more likely to undergo brittle failure.

To reduce the time and costs of future mechanical testing, constitutive models are applied to represent the mechanical responses and failures of polymers. The constitutive model developed by Bouvard et al. [1] was derived from within a larger deformation kinematics and thermodynamics framework in which physically based internal state variables (ISVs) were selected to accurately represent the underlying physics of the polymer deformation mechanisms. The ISV-based model was developed to account for

the viscoelastic behavior of polymers, the material strain softening and strain hardening, and the time and temperature dependence exhibited by polymers under deformation. The material model has been implemented via a subroutine into ABAQUS Explicit.

A failure criterion can be combined together with a constitutive model in order to simulate material failure. Two ways to predict failure in models are by adding continuum damage to the model to incorporate the material's history [2] or by adding failure criteria. In this work, mechanics based failure criteria from the automotive industry are applied to predict material failure. Over the years, many phenomenological, mechanics based failure criteria have been proposed for modeling failure in polymers and metals [3–11]. For this study, a ductile failure criterion based on equivalent plastic strain and a brittle failure criterion based on maximum principal stress are applied to the model to see if failure is accurately predicted.

Experimental tests have been performed for a project entitled “Model for predicting the strain rate dependence - Impact performance of plastic components” sponsored by the American Chemistry Council (ACC). The main goal of this project is to develop a material database for selected polymeric materials along with constitutive framework which captures the material response and failure of the polymers.

The ultimate goal of this thesis is to characterize the mechanical response of polypropylene and copolymer polypropylene through experimental and numerical means and to explore the failure mechanisms that are associated with these responses. My contribution to the study has been to understand the mechanisms of deformation for the different tests performed, to study the fracture mechanisms from the experimental tests, to build and execute the FEA simulations, and to develop the mapping failure criteria to

predict brittle and ductile failures. Fracture patterns observed in tensile, three point bending, and impact tests are compared to results found in literature. Virgin material samples were also obtained for PP and co-PP by submerging material samples in liquid nitrogen and fracturing the samples in a brittle manner. Ductile and brittle fracture surfaces for both materials are examined using a scanning electron microscope (SEM). ABAQUS is used to construct and mesh the finite element models as well as to obtain the results of the simulation.

The thesis describes the work performed in terms of testing and modeling as follows. Chapter 2 will present the setup of the experimental work performed for material characterization as well as the test results on compressive, tensile, impact, and three point bending tests. Chapter 3 will detail the deformation mechanisms observed in PP and co-PP from the microscopic study of the fracture surfaces from tested material specimens. In Chapter 4, the ISV based model for thermoplastics will be introduced followed by the results of the finite element analysis. The numerical capabilities of the model in terms of material prediction and failure are compared with available test data. Chapter 5 will outline the failure criteria implemented into the model.

## CHAPTER II

### EXPERIMENTAL METHODS AND RESULTS

#### 2.1 Materials

The studied materials, a semicrystalline polypropylene homopolymer (PP1105E1) (PP) and a semicrystalline copolymer polypropylene (PP AXO3BE3) (co-PP), were provided by ExxonMobil. Both of these materials are used for many applications in automobiles, household appliances, and construction industries due to their good stiffness and toughness which are similar to those of other engineering plastics. As a result of the rubber particles distributed throughout the co-PP material matrix, co-PP has a better impact strength, is tougher, and is more durable than PP. Some properties of PP and co-PP are summarized in Table 2.1. Both materials also exhibit similar mechanical responses to loadings.

Table 2.1 Properties of Polypropylene and Copolymer Polypropylene [12-13]

			PP	Co-PP
Property	Units	Conditions	Value	Value
Tensile Strength at Yield	MPa	ASTM D638 51 mm/min	31.6	26
Flexural Modulus	MPa	ASTM D790	1150	1269
Notch Izod Impact	Jm <sup>-1</sup>	ASTM D256A (23°C)	32	91
Deflection Temperature Under Load	°C	ASTM D648	87.7	99

During the crystallization of polymers such as polypropylene and copolymer polypropylene, partial alignment of the molecular chains occurs forming ordered regions called lamellae. These lamellae compose larger spherical structures called spherulites as shown in Figure 2.1(a). When co-PP is crystallizing, the spherulite size, nucleation, and growth rate of the co-PP material are all affected by the impact modifiers added to the matrix. The average spherulite size of PP is around 90  $\mu\text{m}$ , but with the inclusion of a modifier, the spherulite size decreases to around 50  $\mu\text{m}$  [14]. In PP, the boundaries between spherulites are very distinct and clear; however, the boundaries are irregular and difficult to distinguish in the copolymer. Figure 2.1(b) shows an impact PP copolymer with the less distinct boundaries of the spherulites.

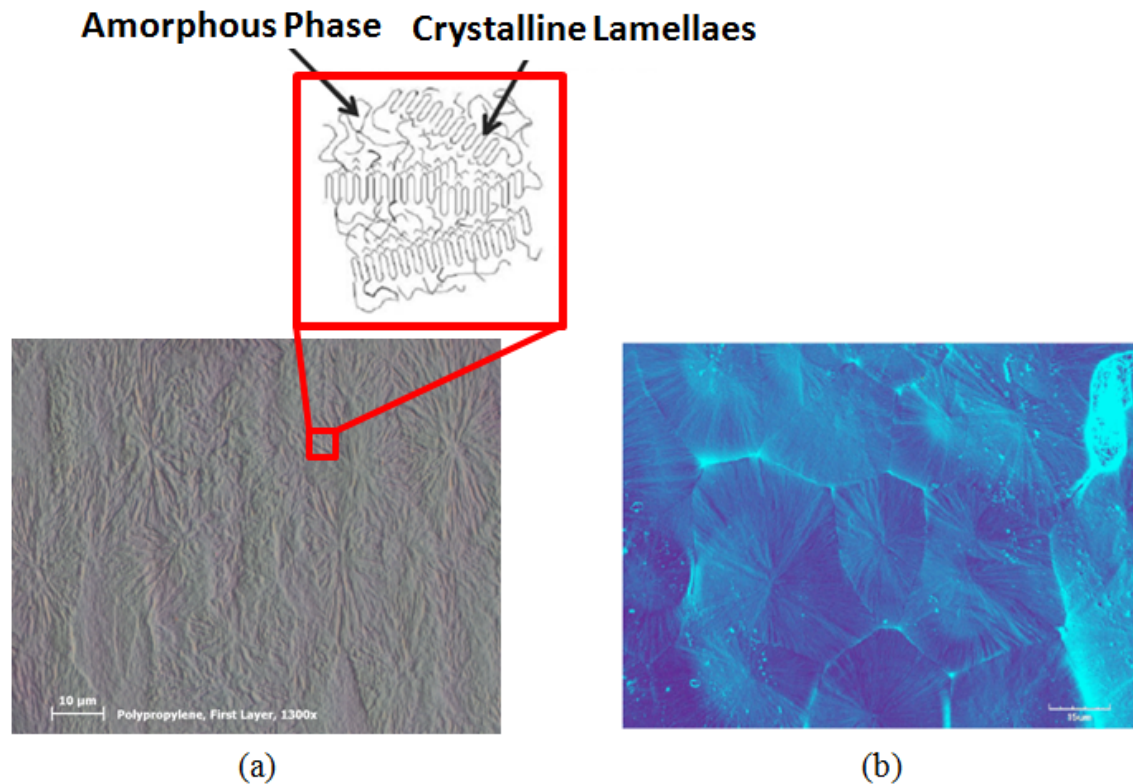


Figure 2.1 Spherulites in (a) PP and (b) impact PP copolymer [15]

## 2.2 Mechanical Testing

Quasi-static compression tests were performed at strain rates of 0.0005, 0.001, 0.01, and 0.1/s and a range of temperatures. The temperatures selected for testing were -20, 25, and 70°C. The tests were performed on an Instron 5882 electro mechanical load frame with an environmental chamber. Tests were conducted in strain rate control using an Instron 25.4 mm extensometer attached to the compression plates. For PP and co-PP, small compression specimens (5 mm diameter and 2.5 mm thickness) were machined from large molded disks. Dry Moly Paste was used for room and high temperature testing, whereas Molykote metal assembly paste was used for low temperature testing

due to its lower viscosity. Each specimen was placed in a heated or cooled environment for 45 minutes at the required temperature prior to testing.

Tensile tests were performed at strain rates of 0.0005, 0.007, 0.1/s for PP and 0.0005, 0.001, and 0.01/s for co-PP. For both materials, the temperatures of -20, 25, and 70°C were selected for testing. Tensile tests were conducted using an Instron 5882 electro mechanical load frame with an environmental chamber and were controlled using the machine cross head speed. Tests were carried out by following ASTM D638-03 on “Standard Test Method for Tensile Properties of Plastics.” The tensile specimen geometry is illustrated in Figure 2.2

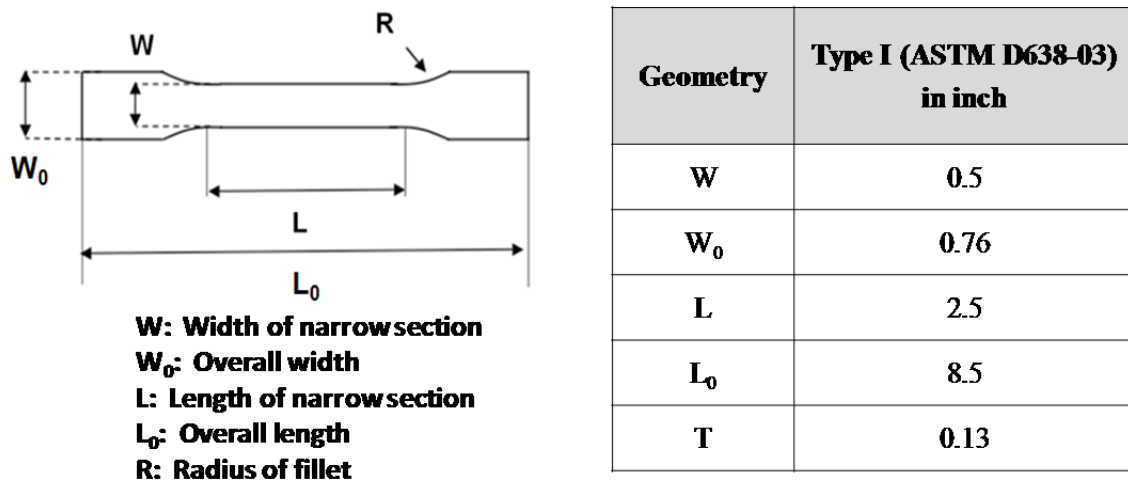


Figure 2.2 Specimen geometry for tension tests (Type I)

Impact tests on PP and co-PP were performed by University of Dayton Research Institute following ASTM test standard D 5628 as displayed in Figure 2.3. Tests were performed at velocities of 0.3, 3, and 30 mm/s at temperatures of -20, 25, and 70°C. The impact tests were conducted on rectangular plaques (100 x 95 x 3 mm) using a MTS



servo-hydraulic 111,200 N load frame with a 48,930 N full scale load cell. The load cell was used for the first and second displacement rates, while a Kistler piezoelectric 90,000 N full scale force washer was used for the third displacement rate. The load measure device was changed because the MTS strain gauged load cell has a slower frequency response time than the Kistler piezoelectric load cell.

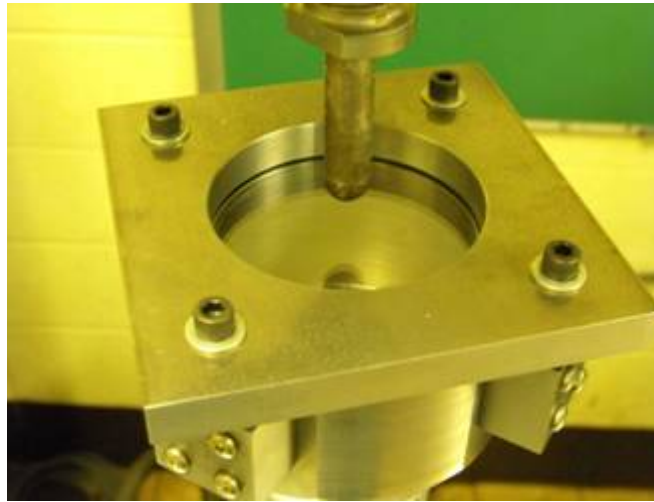
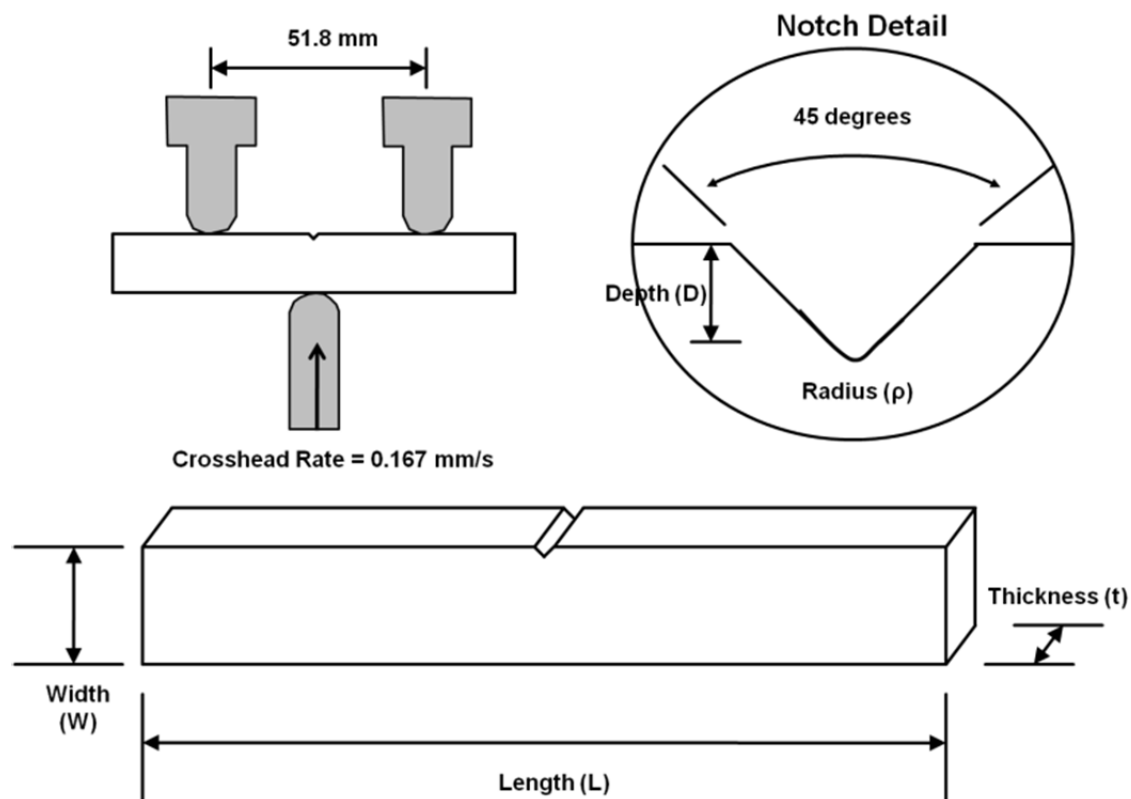


Figure 2.3 Impact test set-up with specimen secured in the fixture

For the three point bending tests, four different geometries of specimens were investigated. For PP and co-PP, two thicknesses were examined. Notched with a notch angle of  $45^\circ$ , two different diameters at the notch root are machined for each thickness. Specimen geometry and dimensions are summarized in Figure 2.4. Three point bending tests were performed using an Instron 5882 electro-mechanical load frame with an environmental chamber. Tests were controlled using the machine cross head speed.



Geometry	PP (mm)	Co-PP (mm)
L	125	63.3
T	3.2 and 5.2	3.17 and 5.69
W	12	12.52
$\rho$	0.19 and 0.79	0.19 and 0.79
D	~3.5	~3.5

Figure 2.4 Three point bending specimen geometry and dimensions

## **2.3 Results of Mechanical Testing**

### **2.3.1 Compression**

Figure 2.5 shows the time and temperature dependent behavior of PP and co-PP in compression. The materials show similar features in their mechanical responses. First, an initial elastic response is present that is considered to be fully recoverable. This is followed by a non-linear transition curve to the yield peak, and after yielding, a decrease in the stress values indicates a material softening. Once crystallographic slip has been initiated by high enough stress levels, crystal plasticity overtakes the control of further deformation process. At larger deformations, strain hardening is induced by the straightening of the entanglement network. This process is displayed in Figure 2.6 which summarizes the deformation mechanisms of an isotactic PP subjected to plane strain compression in a channel die and tensile loading [16].

The yield stress for PP and co-PP depend upon the strain rate and temperature at which they are tested. Higher rates of loading and lower temperatures lead to higher yield stresses. As seen in Figure 2.5, for PP and co-PP, as the applied strain rate is increased, an increase in the yield peak is also seen. The yield stress is higher for PP than co-PP in all strain rates and temperatures investigated. The decrease in yield stress for the copolymer could be a result of the localized plastic deformation of the matrix that occurs at stress concentrations caused by the rubber particles. The values of the yield peaks are comparable to values found in the literature [17-18]. Both materials also experience significant softening as the temperature is increased.

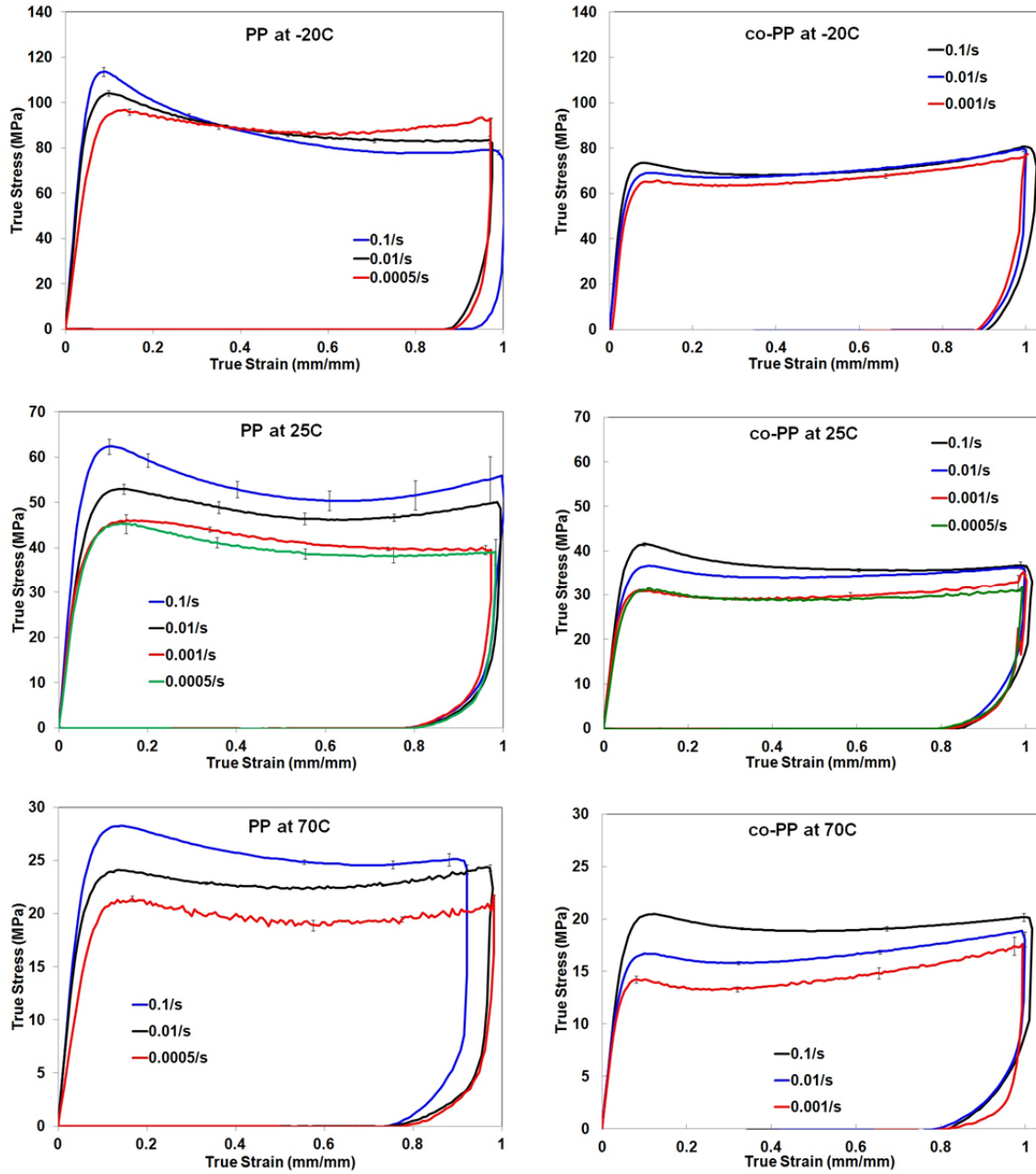


Figure 2.5 Effect of temperature and strain rate on the large strain compressive behavior of PP compared to co-PP

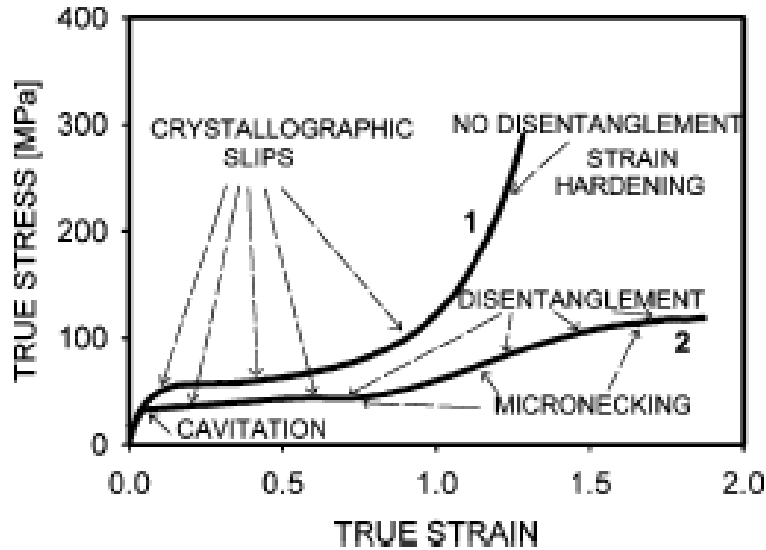


Figure 2.6 Mechanisms associated with the plastic deformation of crystalline polymers explained on the example of isotactic PP: curve 1, channel die compression; curve 2, tensile experiment [16]

### 2.3.2 Tension

The stress-strain curves for PP and co-PP under tension for different strain rates and temperatures are displayed in Figure 2.7. PP shows brittle failure at  $-20^{\circ}\text{C}$  for the three strain rates being tested as well as at  $25^{\circ}\text{C}$  for 0.1/s. At  $25^{\circ}\text{C}$  (for 0.007/s and 0.0005/s) and  $70^{\circ}\text{C}$ , PP experiences ductile behavior with no specimen failure but a significant amount of necking is present. Co-PP shows ductile failure at temperatures of  $-20^{\circ}\text{C}$  and  $25^{\circ}\text{C}$ , while at higher temperatures, co-PP shows ductile behavior by necking. All tests exhibit an initial elastic region, and as the strain increases, the material begins to yield. While the yield stresses are lower for co-PP than PP, the range of yield peak values is in agreement with values reported in the literature [17]. Stress whitening, which is caused by cavitation and crazing, is observed near the fracture surfaces in both PP and co-PP specimens, but the amount of whitening is much greater in co-PP. In co-PP the

length of crazes is much shorter, so the number formed before the specimen fails is significantly greater [19].

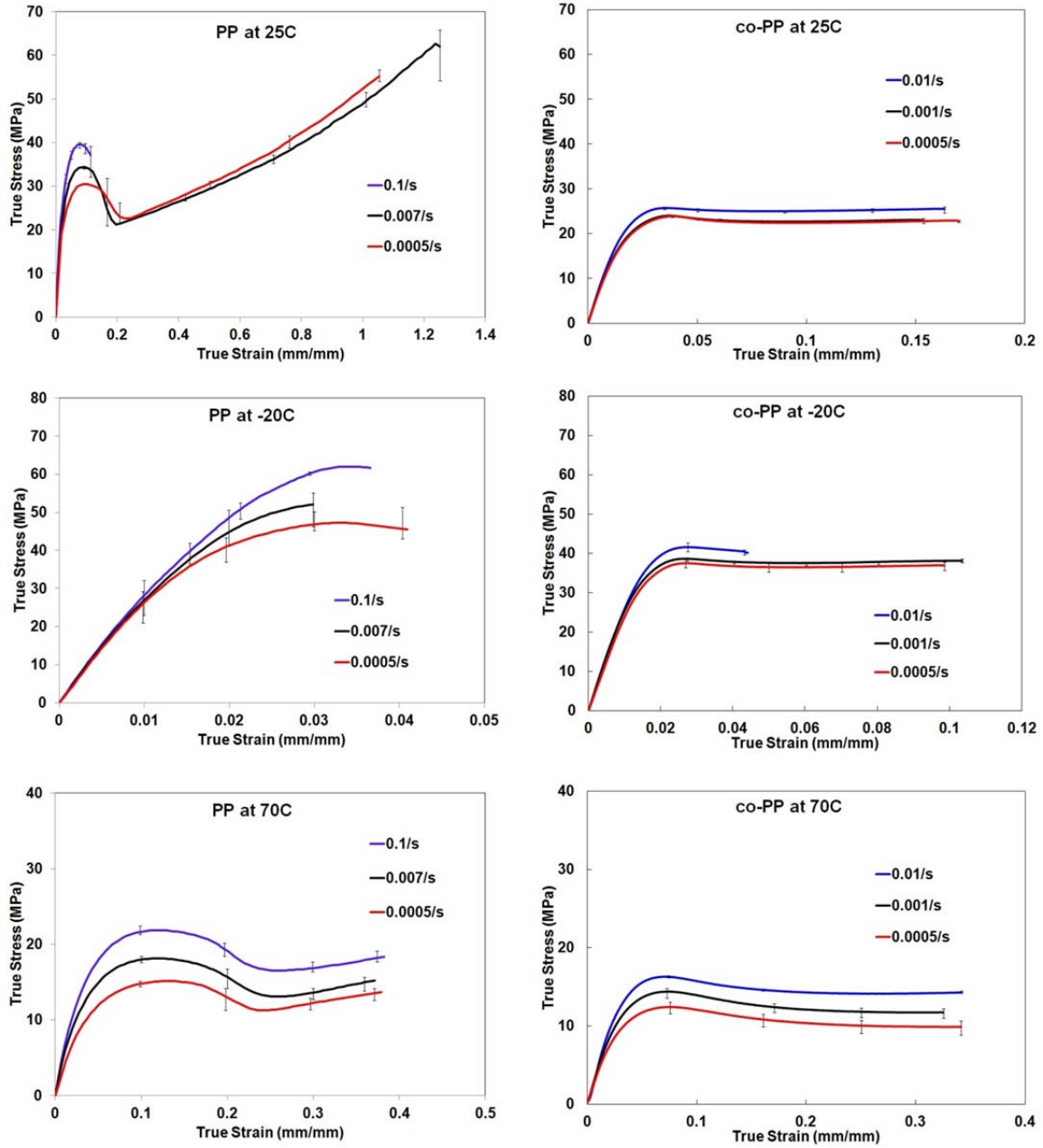


Figure 2.7 Stress-strain curves at different strain rates and temperatures for PP and co-PP

In the previous section, Figure 2.6 demonstrates the mechanisms present during tensile loading. For tensile tests, the stress level at yield may be associated with the onset of cavitation instead of the onset of plastic deformation of crystals. At higher strains, the cavitation pores extend in the direction of the loading and the material between the pores begins to deform plastically, including crystal plasticity mechanisms, and leading to micronecking. While cavitation and micronecking are occurring, chain disentanglement causes the entanglement network to loosen and limits the strain hardening [16].

### **2.3.3 Impact**

The force-displacement curves for impact tests on PP and co-PP at three different velocities (0.3, 3, and 30 mm/s) and three temperatures (-20, 25, and 70°C) are displayed in Figure 2.8. PP shows brittle failure at -20°C and ductile failure at 25°C and 70°C, while co-PP shows ductile failure at all three test temperatures. For PP at -20°C, the force-displacement line appears very rough and jagged due to the test results only being recorded to one decimal place. Both PP and co-PP show significant softening as the temperature is increased. As depicted in Figure 2.9, PP and co-PP both show a strong time-dependence with a peak load that increases with the applied displacement velocity.

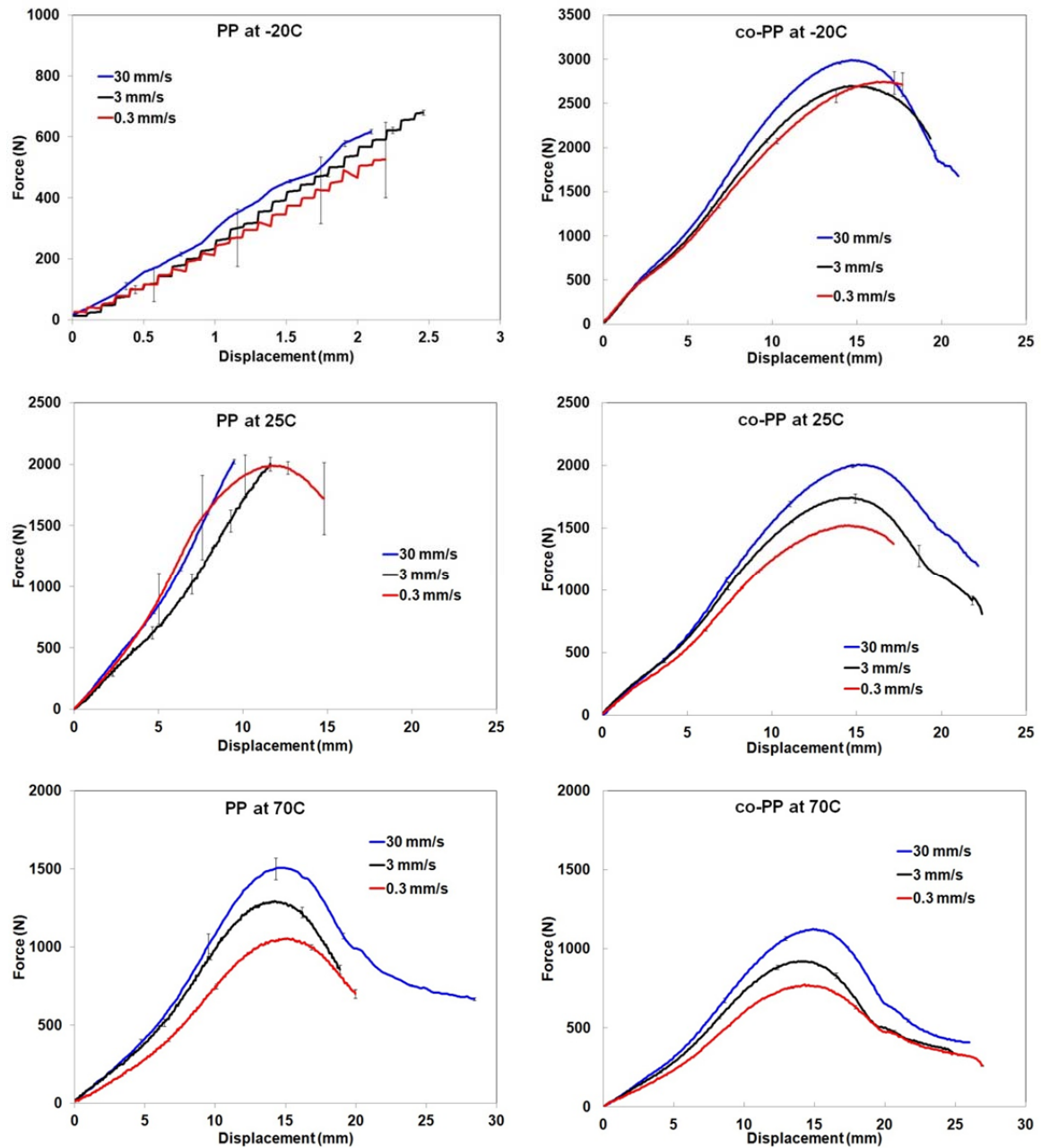


Figure 2.8 Effect of temperature and loading rate for impact tests on PP and co-PP



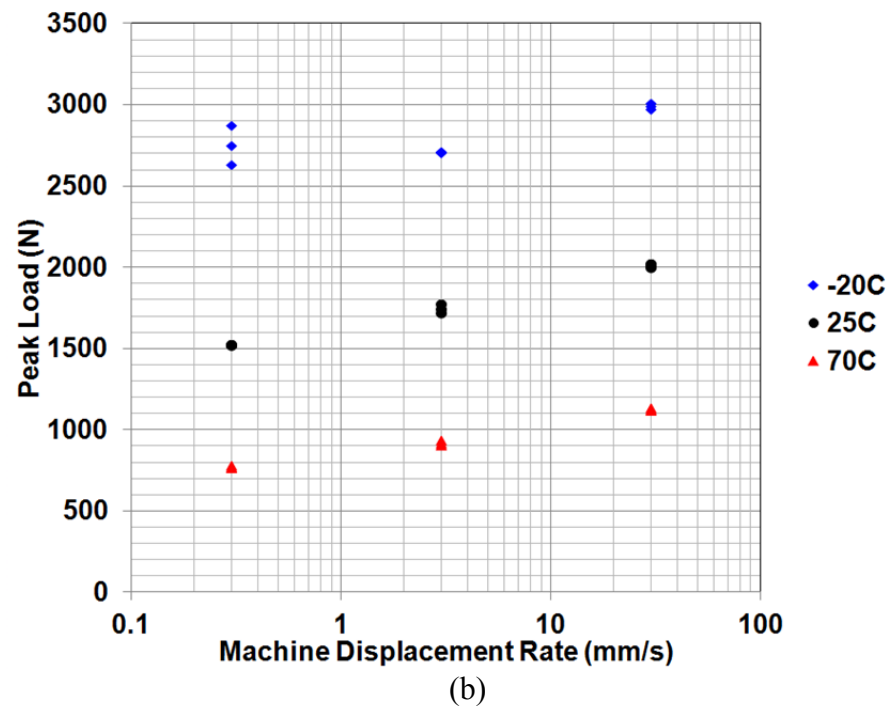
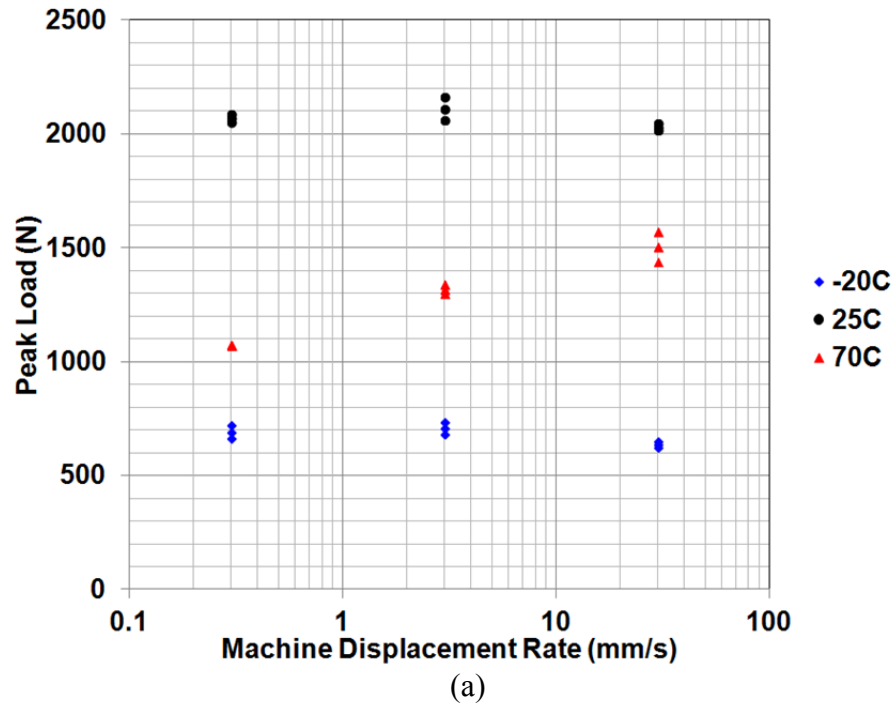


Figure 2.9 Curves of peak load versus displacement for impact tests on (a) PP and (b) co-PP

#### **2.3.4 Three Point Bending**

The three point bending tests allow for the investigation of how the stress concentration induced by different geometries of notch affects the failure modes (i.e. brittle or ductile). Figure 2.10 shows the force-displacement curves for three point bending of PP and co-PP at 0.1667 mm/s at 25°C and 70°C for the four different geometries of specimens. As seen in the figure, PP exhibits brittle failure at 25°C for all specimen geometries and at 70°C only for the small notch-thick specimen. The other geometries for PP show ductile failure at 70°C. For co-PP, all specimen geometries at 25°C and 70°C exhibit ductile failure.

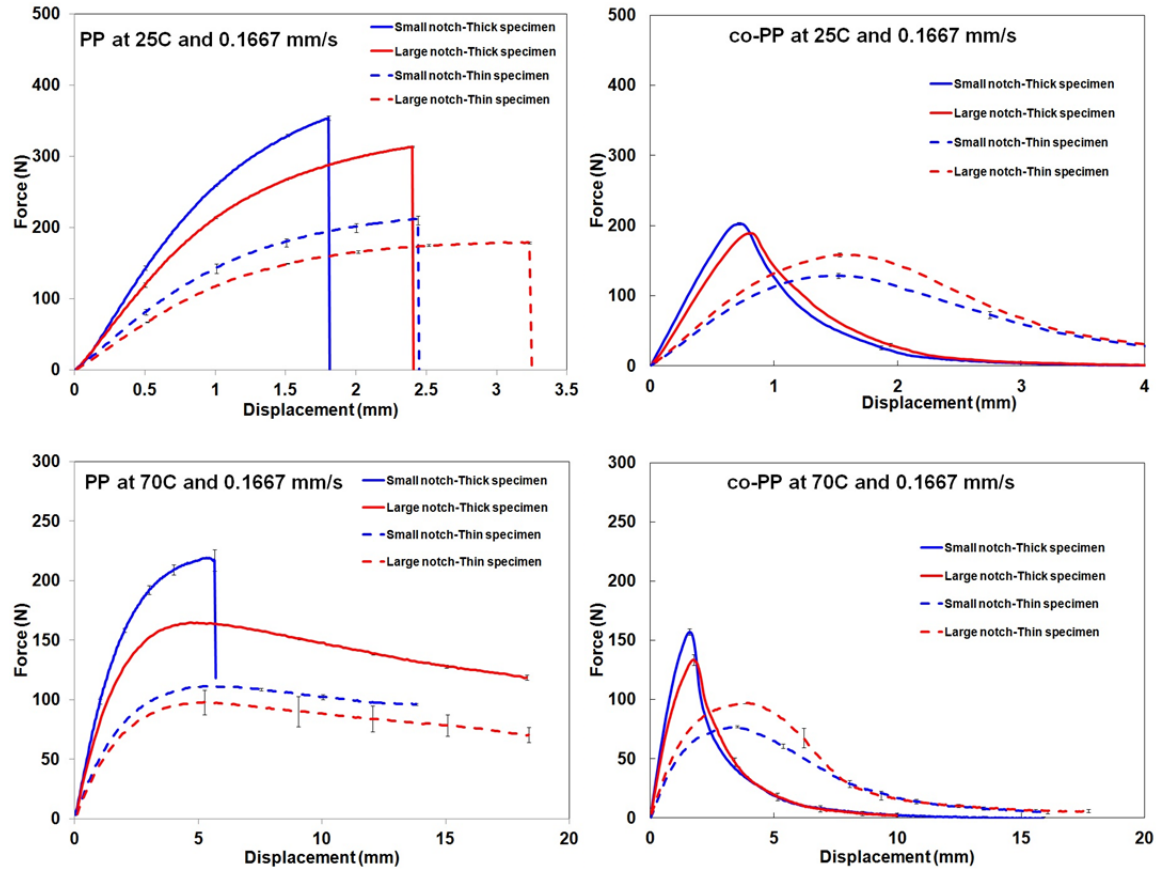


Figure 2.10 Curves of failure load versus displacement for three point bend tests for PP and co-PP

For polypropylene at 25°C and 70°C, the small notch thick specimen possessed the highest peak force and the lowest elongation to failure, while the large notch thin specimen contained the lowest peak force yet the most elongation to failure. This is due to the stress triaxiality formed at the notch of the specimens. The smaller notch and larger thickness impart a higher stress triaxiality on a specimen than the larger notch and smaller thickness.

Co-PP also showed the small notch thick specimen as having the highest peak yet shortest elongation to failure; however, the small notch specimen for co-PP has the

lowest peak force and longest elongation to failure. According to some theories such as the Johnson-Cook damage model, damage is a function of both triaxiality and plastic strain. Assume that for the PP specimens and co-PP thick specimens, triaxiality may dominate and the plastic strain may be negligible. For the co-PP thin geometries, the plastic strain may be more significant and not negligible, thus changing the expected result of the large notch thin possessing the lowest peak force and longest elongation to failure.

## CHAPTER III

### FRACTURE SURFACE MORPHOLOGY

#### **3.1 Specimen Preparation**

When performing SEM on polymers, extra steps must be taken during the preparation of specimens due to the low electrical conductivity of the materials that induces accumulating charges on the surface of the specimen. To reduce this problem, the specimens can be metallicized by sputter coating the specimen in a thin layer of conducting material.

Fracture surfaces of the failed specimens were obtained by first cutting the specimens far away from the fracture surface, and then the non-fracture surface sides of the specimen were painted in a layer of colloidal silver liquid to increase conductivity. The fracture surfaces were then sputter coated in a thin layer of gold before being used in a Zeiss EVO 50 SEM.

#### **3.2 Polypropylene Deformation**

##### **3.2.1 Brittle Failure**

The outer layer of the polypropylene specimens is covered by a thin skin formed by aligned chains without spherulite features. This skin was formed during the injection molding process. Therefore, to observe a virgin microstructure to be used as a reference for the fracture surfaces, an untested, undeformed specimen of PP was placed in liquid

nitrogen and cooled to  $-196^{\circ}\text{C}$  which is well below PP's glass transition temperature of  $10^{\circ}\text{C}$ . Immediately after removing the material sample from the liquid nitrogen, the sample was broken. This structure should correspond to a virgin material surface since no plastic deformation should occur at this low temperature. This procedure was chosen since normal procedures such as polishing the surface may fill cavities that are present or cause thermal damage. Figure 3.1 displays the SEM images of the virgin PP surface.

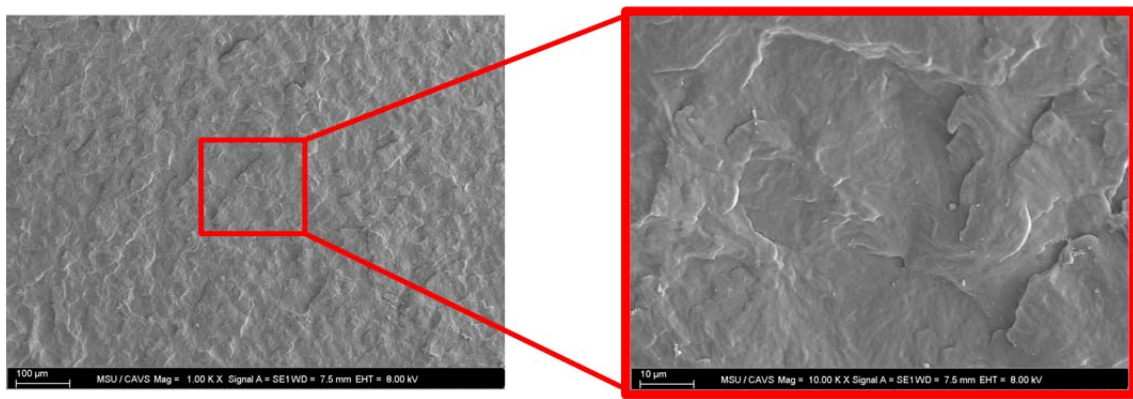


Figure 3.1 SEM images of PP virgin surface

Figure 3.2 shows a fracture surface of a PP tension specimen tested at  $-20^{\circ}\text{C}$  and 0.1/s that experiences brittle failure. At low temperatures, the main deformation process in PP is crazing [14]. Looking across the fracture surface, it seems that multiple craze initiation sites are possible due to the different levels present on the surface. Crazes begin at these different levels within the specimen and then coalesce to form larger flaws, which eventually leads to failure. One such initiation site is shown in the lower blow up in Figure 3.2 and contains radial lines pointing back to a central location.

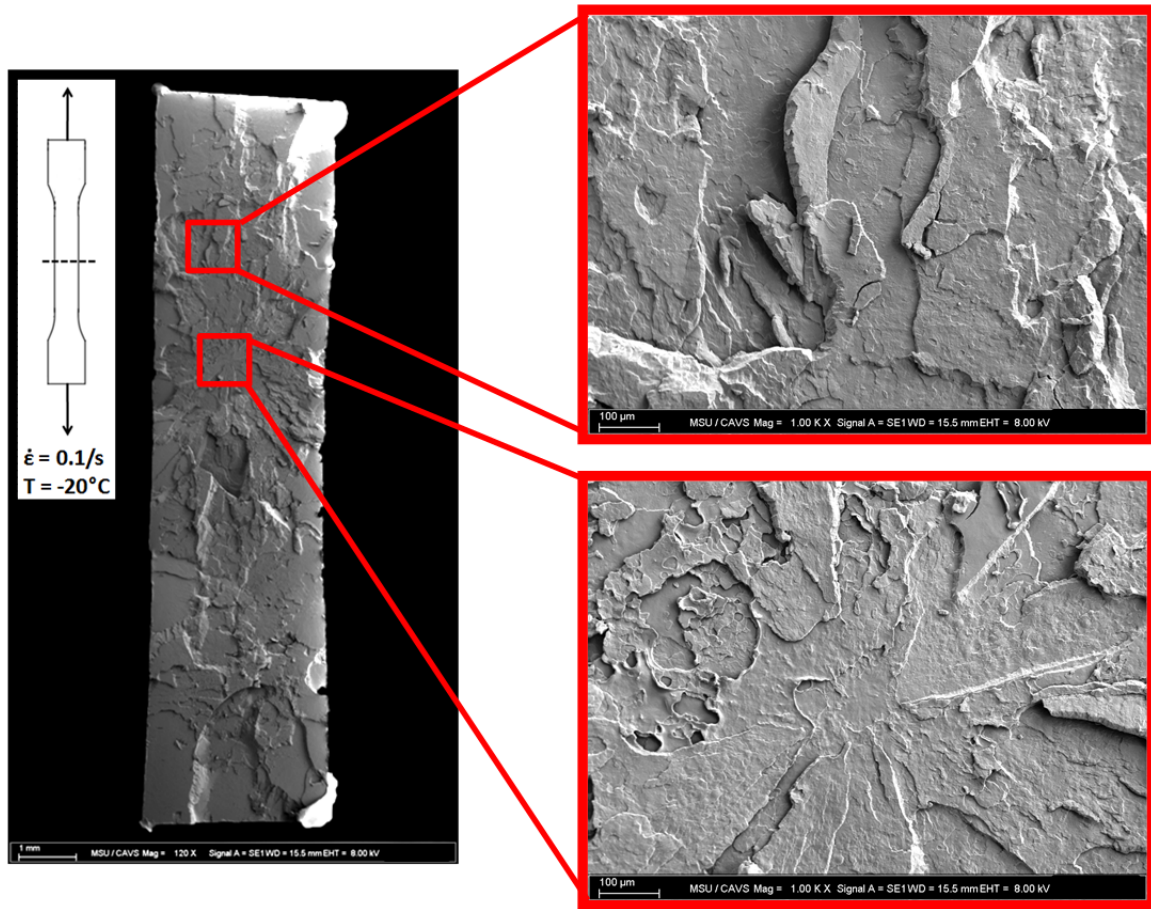


Figure 3.2 Brittle failure of PP tension specimen at -20°C and 0.1/s

Figure 3.3 shows a fracture surface of a PP tension specimen tested at 25°C and 0.1/s that also experiences brittle failure. This brittle fracture surface has different features than the specimen at -20°C. Two separate regions are noticeable: a rough area (left insert) and a smooth area (right insert). The smooth area is very similar in appearance to the brittle virgin fracture surface from Figure 3.1. It should be noted that the upper and lower edges of the fracture surface appear more ductile. This could be the thin skin that covers the outside of the specimens. If this skin tends to tear in a ductile manner, then it could be tougher and lead to a higher elongation to failure. Optical

microscope observations show that the skin was about 100  $\mu\text{m}$  which is in agreement with the thickness of the upper and lower edges observed in Figure 3.3.

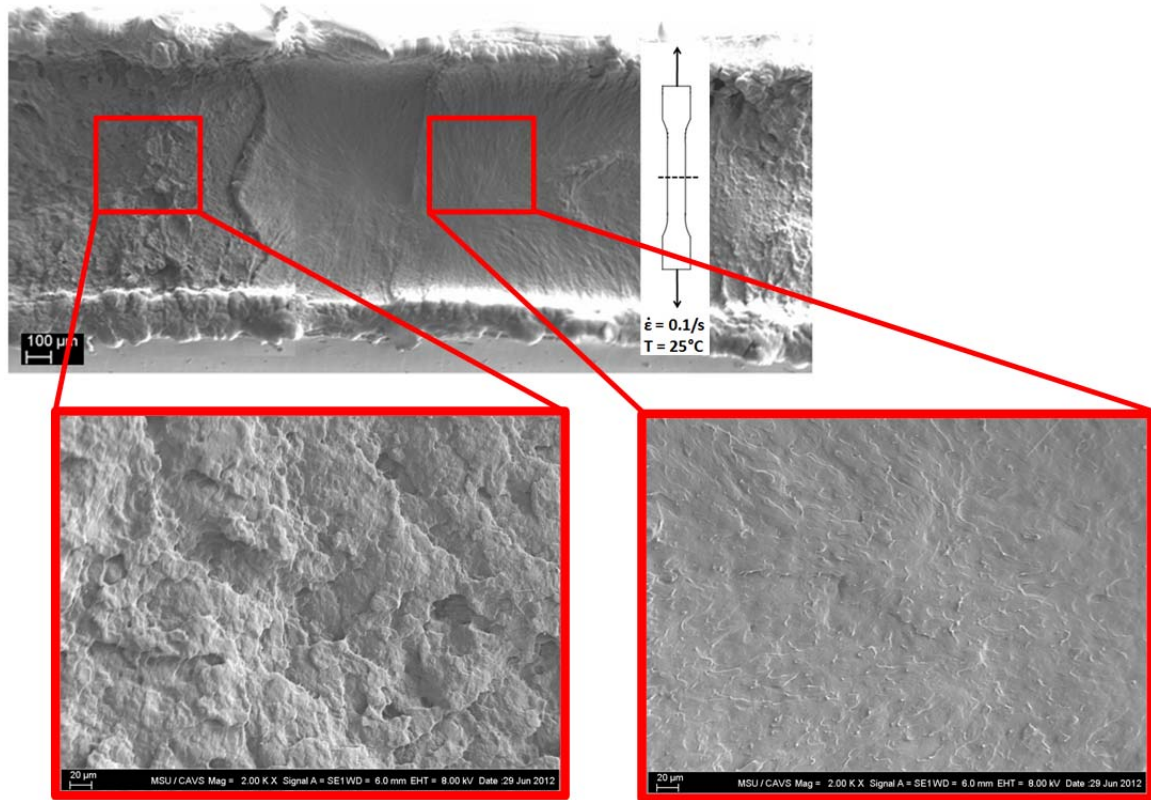


Figure 3.3 Brittle failure of PP tension specimen at 25°C and 0.1/s

At 25°C, all of the PP three point bending specimens experienced brittle failure. A brittle fracture surface of PP under these test conditions usually has three distinct regions, as seen in Figure 3.4 and Figure 3.5. The first region, which is located close to the notch, contains a highly stress-whitened, smooth area. The second region consists of a rough, but un-whitened surface. After the rough surface of the second region, the



fracture surface becomes smooth again, which is the third region. This smoothness is due to unstable crack propagation throughout the region [20].

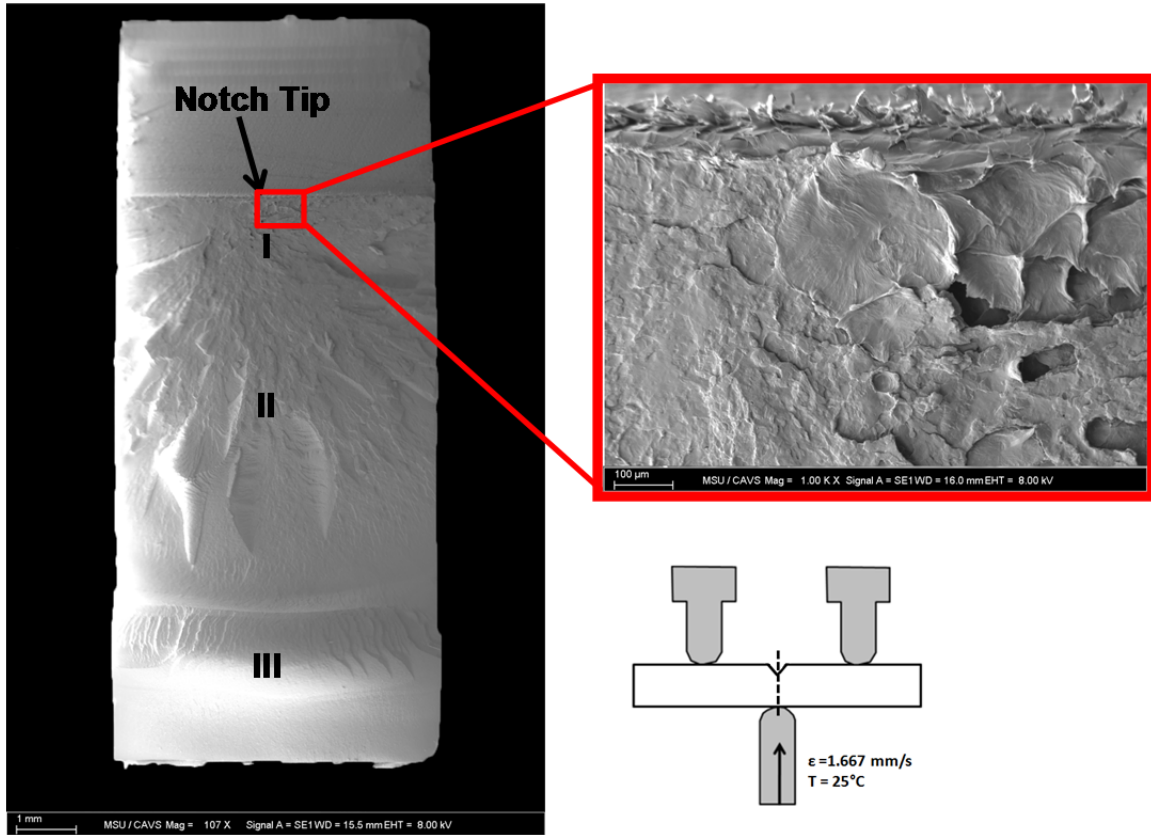


Figure 3.4 Fracture surface of PP small notch thick three point bending specimen at 0.1667 mm/s and 25°C

Figure 3.5 displays the brittle fracture surface of a PP large notch thin three point bending specimen. Like the small notch thick specimen depicted in Figure 3.4, the three different regions of the fracture can be seen.

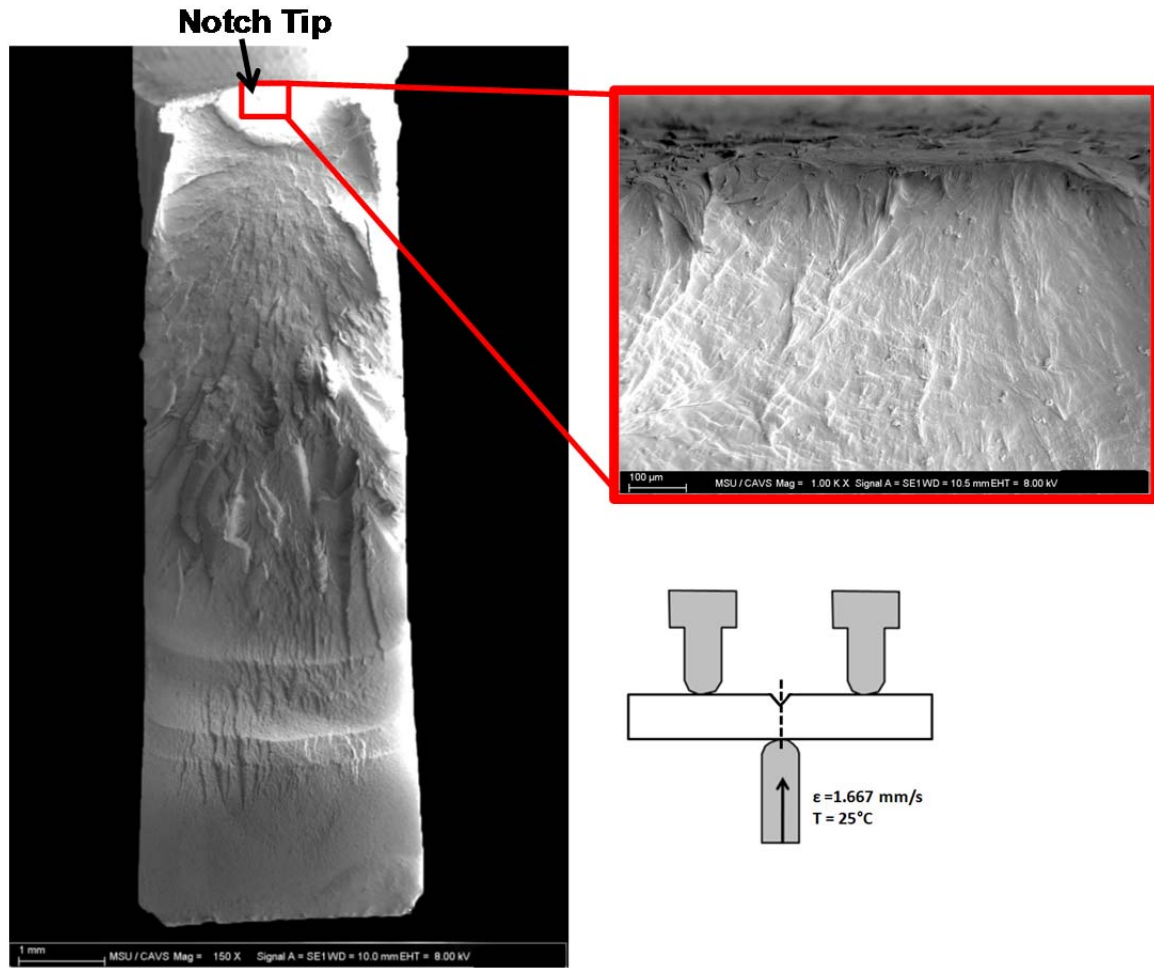


Figure 3.5 Fracture surface of PP large notch thin three point bending specimen at 0.1667 mm/s and 25°C

### 3.2.2 Ductile Failure

Although several PP specimens exhibited ductile behavior, no fracture surfaces of these specimens were produced from tension or three point bending testing. For tension, test specimens at 25°C (for 0.007/s and 0.0005/s) and 70°C displayed ductile behavior with significant amounts of necking, but no fracture occurred. Several three point bending tests at 70°C also exhibited ductile behavior but no fracture. Several of the brittle fracture surfaces discussed in the previous section, such as the small notch thick

and large notch thin three point bend specimens as well as the tension specimen at 25°C and 0.1/s, contained traces of ductile behavior though.

Both the polypropylene small notch thick and large notch thin three point bend specimens shown in Figure 3.4 and Figure 3.5, respectively, show signs of ductile behavior. At the notch of the small notch thick specimen, an area containing traces of ductile behavior can also be seen. The drawing up of the surface on the right side of the image is evidence of ductility, whereas the left side of the image appears to be the flat, smoother surface of a brittle failure. At the notch tip, evidence of tearing is suggested by the many finely tipped pieces of material. In Figure 3.5, the large notch thin specimen contains thinning on the edges near the notch. This shows an increase in ductility as compared to the small notch thick specimen above. Figure 3.6 displays one of these thinning edges next to the notch of the PP large notch thin specimen. The material does not have the same characteristics as the brittle fractures previously examined. Also, several hair like strands of material coming off of the material indicate that stretching and tearing were present in this location.

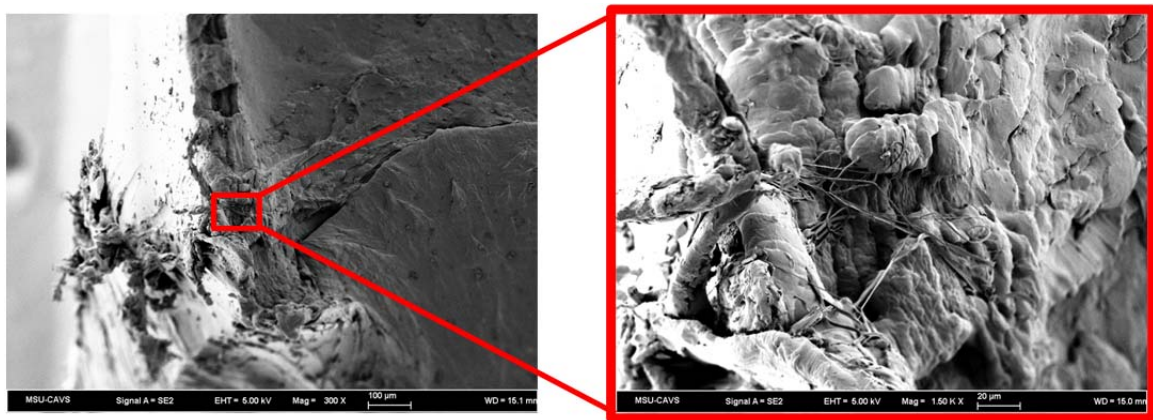


Figure 3.6 Ductile features on a PP large notch thin specimen

The PP tension specimen tested at 25°C and 0.1/s presented in the previous section also showed signs of ductility. While all of the material on the inside appears brittle, the outer edge of the specimen contains features that indicate ductility as seen in Figure 3.7. Like the PP large notch thin edge, the edge does not contain the brittle characteristics that are seen in the other specimens. Again, a stretched piece of material seen on the edge of the fracture surface indicates that tearing and stretching were present during failure. This edge could be composed of the outer skin later that surrounds the PP material. If this skin tends to tear in a ductile manner, this will increase the toughness and elongation to failure of polypropylene.

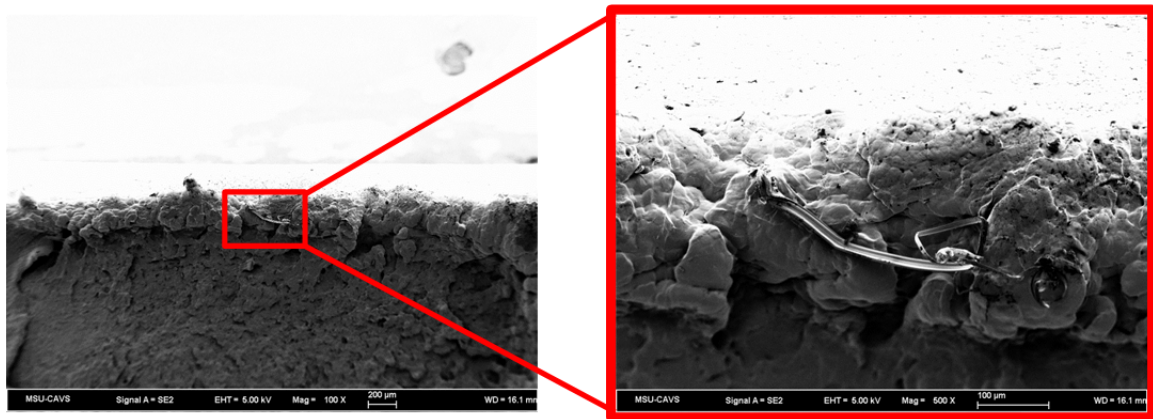


Figure 3.7 Ductile features on the edge of a PP tension specimen tested at 25°C and 0.1/s

### 3.3 Copolymer Polypropylene Deformation

#### 3.3.1 Brittle Failure

Just like polypropylene, copolymer polypropylene is covered with an outer layer of skin. Because of this, a co-PP virgin microstructure was created by placing an untested, undeformed co-PP specimen in liquid nitrogen, cooled to -196°C, and then

broken so that no plastic deformation is present on the surface. Again, normal procedures such as polishing the surface may affect certain features or cause thermal damage. Figure 3.8 displays the SEM images of the undeformed, virgin co-PP surface. The overall surface appears very similar to the virgin PP surface; however, several objects of varying size can be seen on the surface.

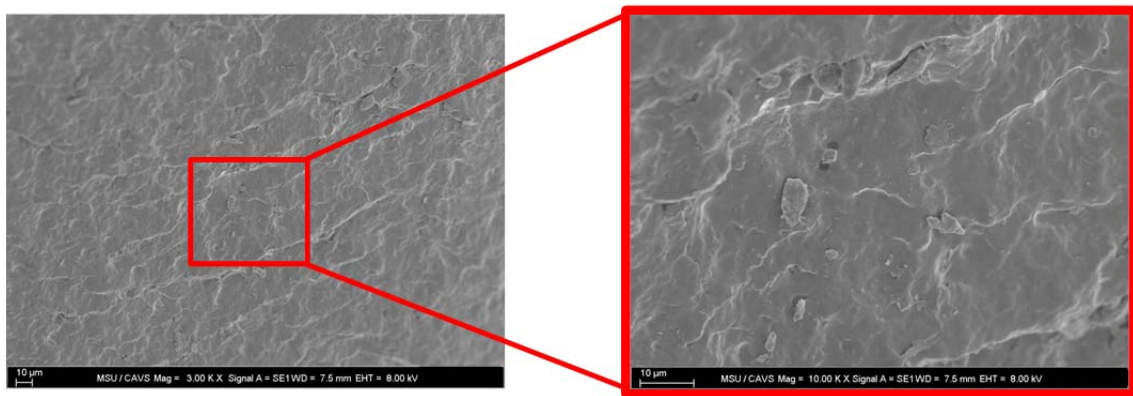


Figure 3.8 SEM images of co-PP virgin surface

### 3.3.2 Ductile Failure

The fracture surface of a co-PP tension specimen tested at 25°C and 0.01/s contained two distinct regions as seen in Figure 3.9. The first region is a ductile area in the center of the fracture surface and is the initiation area where the fracture started. The area can be identified by the long, pulling ligaments that dominate the surface. Outside of this ductile region, the surface appears more brittle and many voids are present. Many of these voids are created by the rubber or inclusions in the co-PP material matrix. Figure 3.10 shows the fracture surface of the ductile failure of a co-PP tension specimen at -20°C and 0.01/s. The surface features of this specimen are very similar to those in Figure 3.9. In the initiation site, smaller pulling ligaments are seen. Void formation is



present throughout the whole fracture surface although not in lesser quantity than the specimen at room temperature.

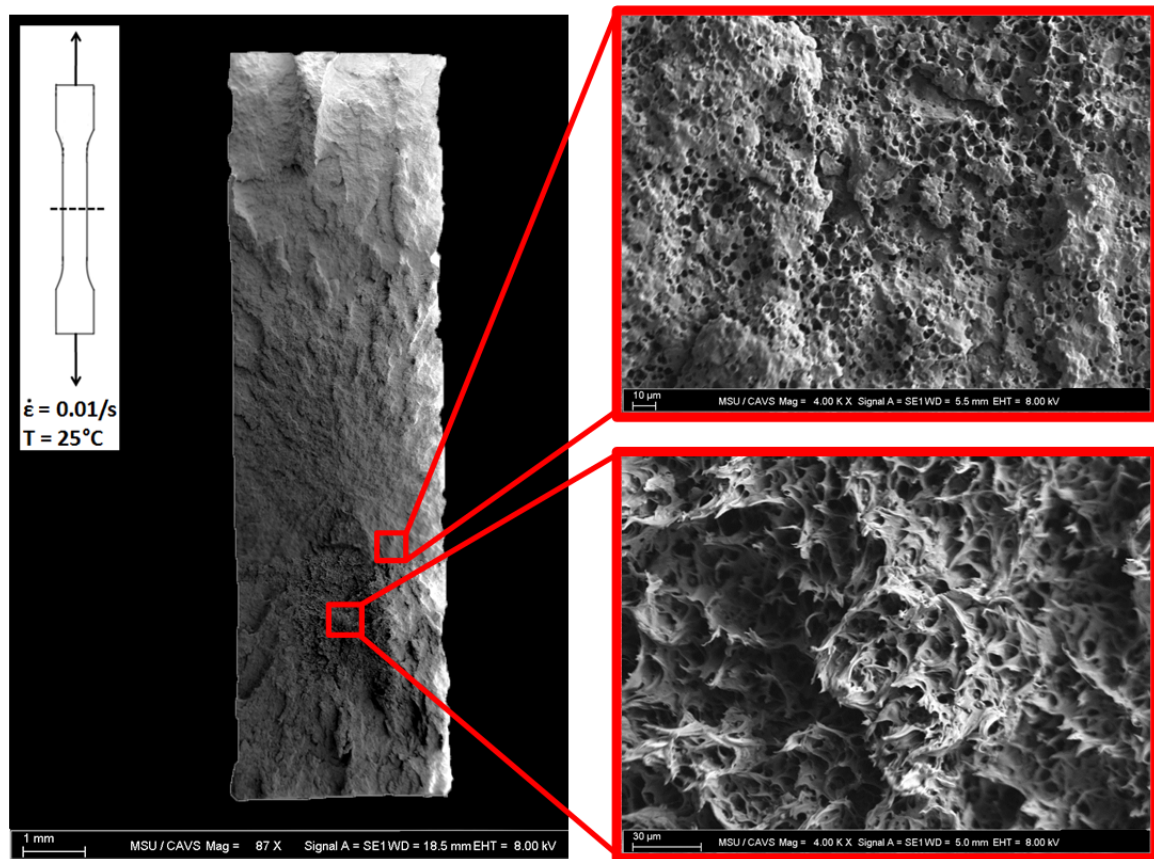


Figure 3.9 Fracture surface of co-PP tension specimen at 25°C and 0.01/s

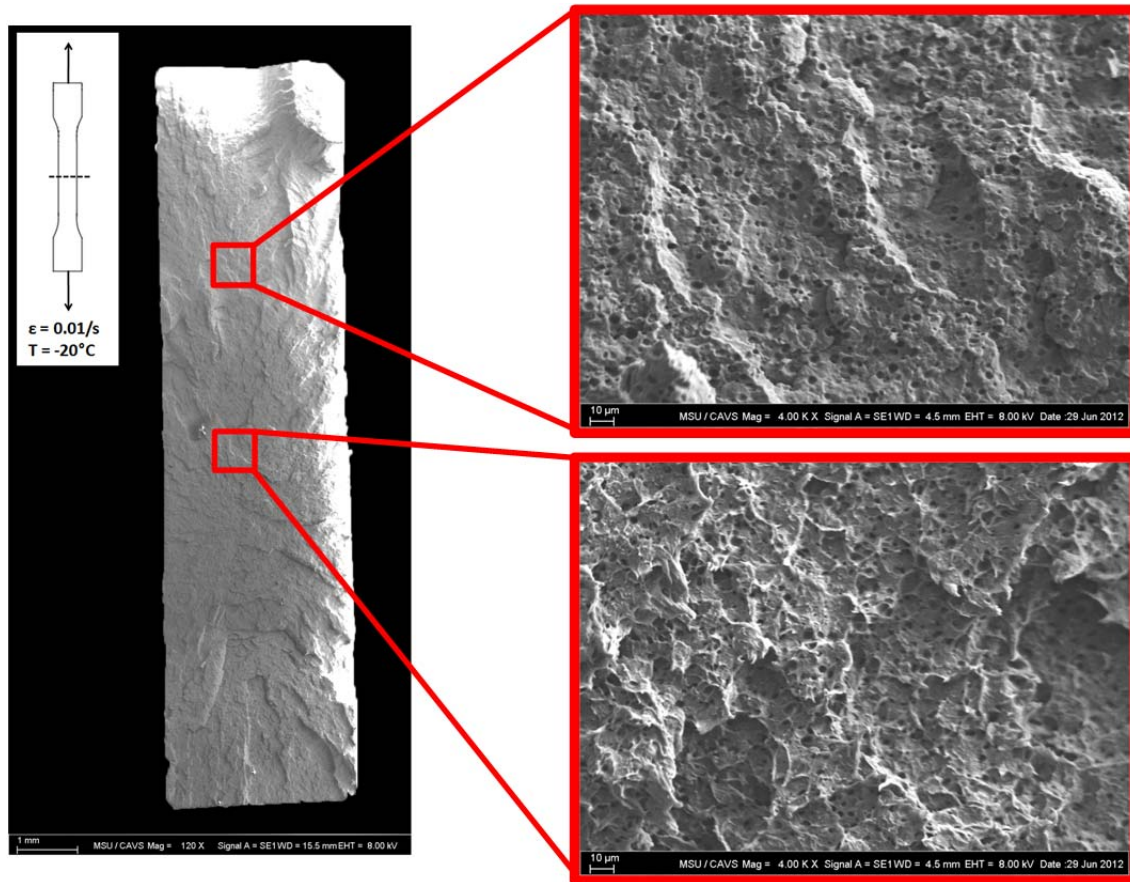


Figure 3.10 Ductile failure of a co-PP tension specimen at  $-20^{\circ}\text{C}$  and  $0.01/\text{s}$

All of the co-PP three point bending specimens experienced ductile failure. The fracture surfaces of the co-PP specimen are relatively smooth and show significant stress whitening. Figure 3.11 and Figure 3.12 display images taken with a SEM of a co-PP small notch thick specimen and small notch thin specimen, respectively. For many toughened polymers, the damage zone located around the notch tip is dominated by microvoids as is seen in the co-PP specimens. Many of these microvoids are a result of cavitation, but particle debonding also contributes to the formation of the voids [21]. Cavitation may take place inside a rubber particle when the bond between the rubber particle and the material matrix is strong enough to resist deformation. However, when

the rubber and matrix are not strongly bonded, interfacial debonding can occur [22]. The small notch thick specimen does not deform as the small notch thin specimen. This is explained by significant tearing that is present on the surface of the small notch thin specimen. Greater amounts of tearing means more energy is required to reach failure. This results in longer elongations to failure but a lower stress values as seen in the experimental results as displayed in Figure 2.10.

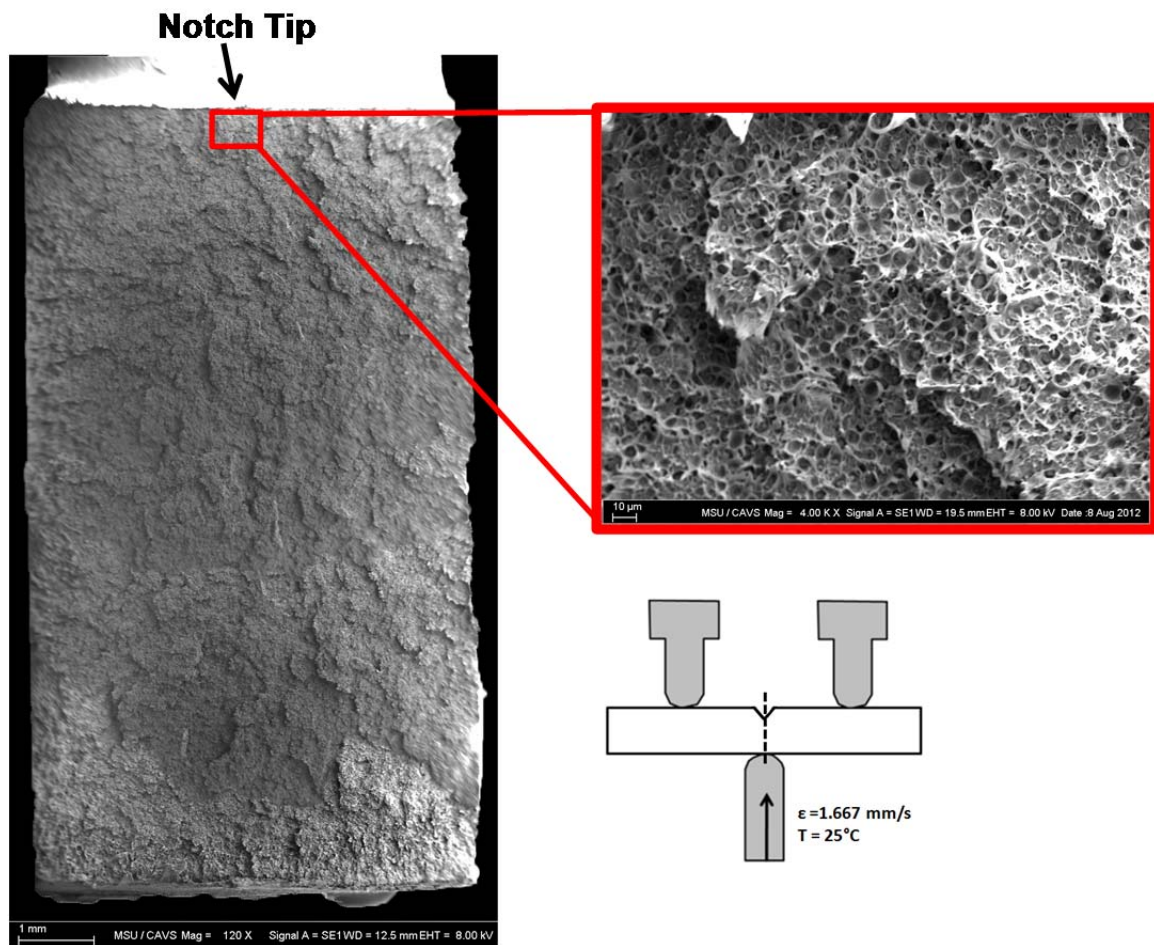


Figure 3.11 Small notch thick three-point bending test specimen for co-PP at 0.1667 mm/s and 25°C



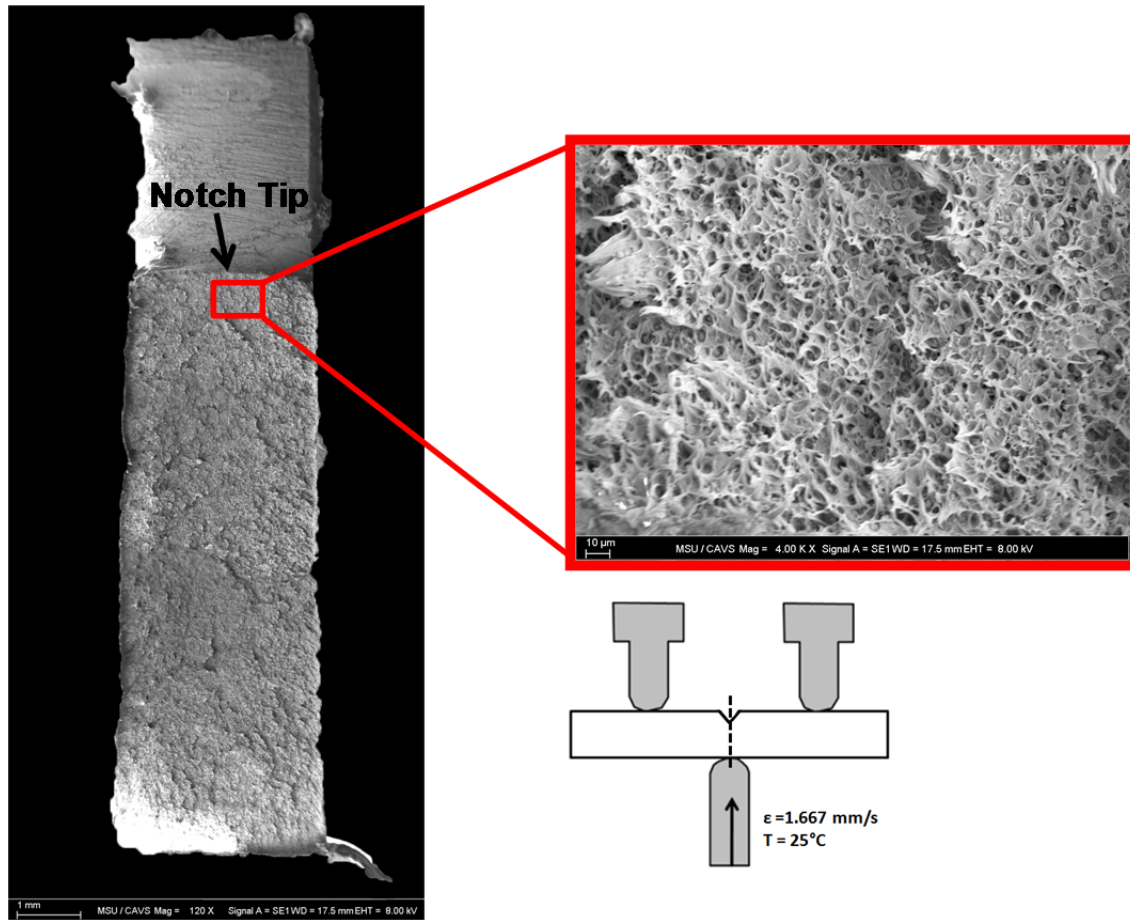


Figure 3.12 Small notch thin three-point bending test specimen for co-PP at 0.1667 mm/s and 25°C

### 3.3.3 Quantitative Microstructure Characterization

Area fraction, number density, size distribution, and nearest neighbor distance distribution of voids are important microstructural parameters of interest in microstructure investigations. The microstructure-property model to characterize damage is a function of these parameters:

$$\Phi = \eta \nu C \quad (\text{Eq. 1})$$

where  $\Phi$  is the volume fraction of the voids,  $\eta$  is related to the number density of the voids,  $v$  is related to the size distribution of the voids, and  $C$  is related to nearest neighbor distribution of the voids.

These parameters were quantified on the fracture surface of a co-PP tension and three point bending specimens using ImageJ. When studying damage or failure of a material, microstructure properties, such as voids, need to be quantified; therefore, it is important to accurately measure these microstructural parameters. Table 3.1, Table 3.2, and Table 3.3 display the averages and standard deviations of the void number density, void size distribution, and distance between a void and its nearest neighbor on one region of the fracture surface.

Table 3.1 Microstructure Property Quantification of a Co-PP Tension Specimen at 25°C and 0.0005/s

	Mean	S <sub>D</sub>
$\eta$	0.015809	0.000947
$v$	3.645	0.263044
$C$	4.056528	0.004311

Table 3.2 Microstructure Property Quantification of a Co-PP Tension Specimen at -20°C and 0.01/s

	Mean	S <sub>D</sub>
$\eta$	0.01545	0.00246
$v$	3.34921	0.21211
$C$	4.43835	0.37882

Table 3.3 Microstructure Property Quantification of a Co-PP Small Notch Thin Three Point Bending Specimen at 25°C and 0.1667 mm/s

	Mean	S <sub>D</sub>
<b>η</b>	0.01911	0.00651
<b>v</b>	3.86509	0.5761
<b>C</b>	4.1627	0.85804

## CHAPTER IV

### NUMERICAL SIMULATIONS

#### 4.1 Model for Thermoplastics

Polymers exhibit a rich variety of material behavior which is both temperature and rate dependent. Such behavior is mainly due to their particular microstructures. To capture this wide range of responses, a number of constitutive models have been developed and presented in the open literature. In particular, many physically-based constitutive equations based on differential formulations using ISVs have been proposed. An ISV material model was developed by Bouvard et al [1] to capture the time and temperature dependent mechanical behavior of thermoplastics characterized by an elastic regime followed by a yield peak, then strain softening and subsequent strain hardening at high strain level. A hierarchical multiscale approach was used to compute and understand the structure-property relations at lower scales in order to develop the continuum level constitutive model. The main purpose of this model is to develop a physically-based, constitutive model framed in a thermodynamic setting. Table 4.1 gives a summary of the three dimensional model.

Table 4.1 Three dimensional model summary

**Cauchy Stress**

$$\blacktriangleright \quad \boldsymbol{\sigma} = \mathbf{J}^{e-1} \boldsymbol{\tau} = \mathbf{J}^{e-1} \mathbf{R}^e \bar{\mathbf{M}} \mathbf{R}^{eT}$$

$$\bar{\mathbf{M}} = 2\mu(\theta, \dot{\epsilon}) \bar{\mathbf{E}}^e + \left( K(\theta, \dot{\epsilon}) - \frac{2}{3} \mu(\theta, \dot{\epsilon}) \right) \text{Tr}(\bar{\mathbf{E}}^e) \bar{\mathbf{I}}$$

$$\mu(\theta, \dot{\epsilon}) = \frac{E(\theta, \dot{\epsilon})}{(2 + 2\nu)}, \quad K(\theta, \dot{\epsilon}) = \frac{2\mu(\theta, \dot{\epsilon})(1 + \nu)}{3(1 - 2\nu)}$$

$$E(\theta) = (E_{\text{ref}} + E_1(\theta - \theta_{\text{ref}})) \left( 1 + \frac{\text{VE1}}{1 + \exp \left[ -\frac{\log(\dot{\epsilon}) - \log(\dot{\epsilon}_{\text{ref}})}{\text{VE2}} \right]} \right)$$

**Internal State Variables**

$$\blacktriangleright \quad \bar{\kappa}_1 = c_{\kappa_1}(\theta) \bar{\xi}_1; \quad c_{\kappa_1}(\theta) = \alpha_1 Z(\theta)$$

$$\dot{\bar{\xi}}_1 = h_0 \left( 1 - \frac{\bar{\xi}_1}{\bar{\xi}^*} \right) \dot{\bar{\gamma}}^p \quad \text{with} \quad \dot{\bar{\xi}}^* = (\bar{\xi}_{\text{sat}}^* - g_0(\theta) \bar{\xi}^*) \dot{\bar{\gamma}}^p$$

$$g_0(\theta) = C_9(\theta - \theta_{\text{ref}}) + C_{10}, \quad \bar{\xi}_0^*(\theta) = C_5(\theta - \theta_{\text{ref}}) + C_6,$$

$$\bar{\xi}_{\text{sat}}^*(\theta) = C_7(\theta - \theta_{\text{ref}}) + C_8$$

$$\blacktriangleright \quad \bar{\kappa}_2 = c_{\kappa_2}(\theta) \bar{\xi}_2; \quad c_{\kappa_2}(\theta) = \alpha_2 \mu(\theta)$$

$$\dot{\bar{\xi}}_2 = h_1 (\bar{\lambda}^p - 1) \left( 1 - \frac{\bar{\xi}_2}{\bar{\xi}_{2\text{sat}}(\theta)} \right) \dot{\bar{\gamma}}^p$$

$$\bar{\xi}_{2\text{sat}}(\theta) = C_{11}(\theta - \theta_{\text{ref}}) + C_{12}$$

Table 4.1 (Continued)

$\triangleright \quad \bar{\alpha} = \hat{\mu}_B(\theta)\bar{\beta} ; \quad \hat{\mu}_B(\theta) = \mu_R(\theta) \left[ 1 - \frac{\lambda_1^{\bar{\beta}} + \lambda_2^{\bar{\beta}} + \lambda_3^{\bar{\beta}} - 3}{\lambda_L} \right]^{-1}$ $\mu_R(\theta) = C_1(\theta - \theta_{\text{ref}}) + C_2$ $\dot{\bar{\beta}} = R_{s_1}(\theta)(\bar{\mathbf{D}}^p \bar{\beta} + \bar{\beta} \bar{\mathbf{D}}^p)$ $R_{s_1}(\theta) = C_{13}(\theta - \theta_{\text{ref}}) + C_{14}$
<p><b><u>Flow rule</u></b></p> $\triangleright \quad \dot{\mathbf{F}}^p = \bar{\mathbf{D}}^p \mathbf{F}^p ; \quad \bar{\mathbf{D}}^p = \frac{1}{\sqrt{2}} \dot{\gamma}^p \bar{\mathbf{N}}^p$ $\dot{\gamma}^p = \dot{\gamma}_0^p e^{\left[ \frac{\Delta H_p}{R\theta} \right]} \left[ \sinh \left( \frac{\bar{\tau}_{\text{eq}} V}{2k_B \theta} \right) \right]^m$ $\bar{\tau} = 1/\sqrt{2} \  \mathbf{DEV}(\bar{\mathbf{M}} - \bar{\alpha}) \  ; \quad \bar{\tau}_{\text{eq}} = \bar{\tau} - (Y(\theta) + \bar{\kappa}_1 + \bar{\kappa}_2 + \alpha_p \bar{\pi})$ $Y(\theta) = C_3(\theta - \theta_{\text{ref}}) + C_4$

The 3D constitutive equations of the model were implemented in ABAQUS/Explicit using a user material subroutine (VUMAT). The developed constitutive model was applied to PP and co-PP under compression, tension, impact, and three point bending tests at different temperatures and strain rates. A MATLAB fitting routine was used to determine the parameter values for these different materials, and they are listed in Table 4.2.

Table 4.2 Parameter identification for 3D model for PP and co-PP

Regime	Parameters	Constants	PP	co-PP
<b>Elasticity</b>	E	$E_{\text{ref}}$ (MPa)	1800	1300
		$E_1$ (MPa/K)	-15.0	-20.0
		$\theta_{\text{ref}}$ (K)	298	298
		A	0.	0.
		B	0.01	0.01
		$\dot{\epsilon}_{\text{ref}}$ (/s)	1000	1000
	$\nu$		0.36	0.36
<b>Viscoplasticity</b>		$\dot{\gamma}_0^p$ (1/s)	$4.5 \times 10^{17}$	$1.819 \times 10^{17}$
		$\Delta H_p$ (KJ/mol)	109.0	109.0
		V (m <sup>3</sup> )	$1.097 \times 10^{-27}$	$1.097 \times 10^{-27}$
		m	3.0	5.08
	Y	$C_3$ (MPa.K <sup>-1</sup> )	-0.15	-0.1
		$C_4$ (MPa)	10.0	8.5
		$\alpha_p$	0.26	0.144
<b>Softening (ISV1)</b>		$h_0$	15.0	19.0
	$\bar{\xi}_0^*$	$C_5$ (/K)	-0.001	-0.009
		$C_6$	0.66	0.66
	$\bar{\xi}_{\text{sat}}^*$	$C_7$ (/K)	-0.0001	0.
		$C_8$	0.43	0.2
	$g_0$	$C_9$ (/K)	-0.01	0.
		$C_{10}$	1.7	2.85
	$C_{\kappa_1}$	$\alpha_{\kappa_1}$	$2.22 \times 10^{-2}$	$1.0 \times 10^{-2}$
<b>Hardening (ISV2)</b>		$h_1$	2.8	2.8
		$\bar{\xi}_{20}$	0.	0.
	$\bar{\xi}_{2\text{sat}}$	$C_{11}$ (/K)	-0.0015	-0.0015
		$C_{12}$	0.699	0.699
	$C_{\kappa_2}$	$\alpha_{\kappa_2}$	0.	0.

Table 4.2 (Continued)

<b>Hardening (ISV3)</b>		$\lambda_L$	4.8	4.8
	$\mu_R$	$C_1$ (MPa/K)	0.	-0.06
		$C_2$ (MPa)	0.	2.0
	$R_{SI}$	$C_{13}$ (/K)	0.	$-7.0 \times 10^{-3}$
		$C_{14}$	0.	0.6
<b>Physical Parameters</b>		$\alpha_{th}$ (/K)	$9.05 \times 10^{-5}$	$9.05 \times 10^{-5}$
		$\omega$	0.	0.
		$\rho$ (t/mm <sup>3</sup> )	$9.05 \times 10^{-10}$	$9.05 \times 10^{-10}$
		$C_v$ (mJ/tK)	$2.0 \times 10^9$	$2.0 \times 10^9$

## 4.2 Finite Element Analysis Model

The geometries and boundary conditions of the tensile, impact, and three point bending simulations are located in Appendix B. To verify that the solution of the numerical analysis has converged, a mesh refinement study is conducted to understand the impact of mesh size on the simulation results. The mesh refinement study for the tensile simulation was completed prior to my work, but I verified the mesh for the three point bending. To verify the convergence of solution using the coarse mesh (see Figure 4.1), the number of elements contained around the notch was doubled to produce the fine mesh (see Figure 4.1). The simulations performed comparing the coarse and fine meshes were performed using the material model for an amorphous polymer, polycarbonate. The results of the polycarbonate simulations containing the two meshes are displayed in Figure 4.2. No difference is observed between the two solutions can be seen, so the coarse mesh around the notch will be used for the three point bending model.



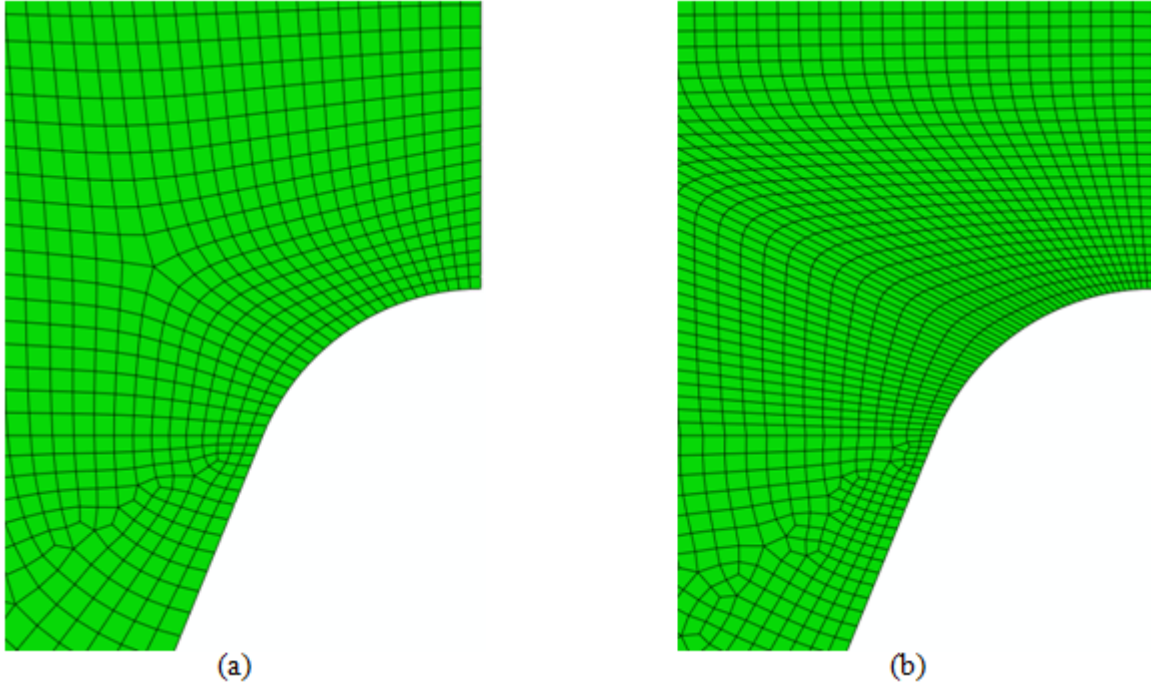


Figure 4.1 (a) Coarse mesh and (b) fine mesh at notch of three point bending model using C4D8R elements

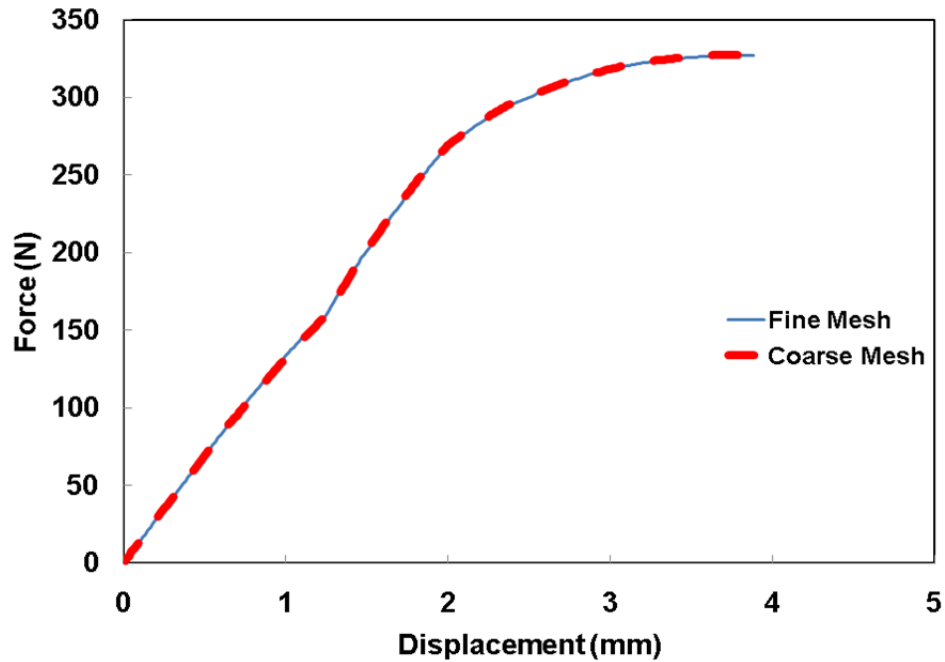


Figure 4.2 Mesh refinement results of three point bending model (Polycarbonate)

A point of inflection can be seen in the results of the mesh refinement study when using the hexahedral C4D8R elements. To get rid of this unwanted inflection point in the simulation solution, the model was remeshed using tetrahedral elements, C3D10M, as seen in Figure 4.3. The results of the simulation using the tet elements is shown in Figure 4.4 along with the comparison to the experiment results as well as the simulation results using the hex elements that contains the inflection point. The inflection point when using the hex elements could have been due to an excessive distortion of elements in the notch area due to stress concentrations that the tet elements did not experience. No inflection point was seen when using the new element, therefore, C3D10M tet elements were used for further modeling of the three point bending simulations.

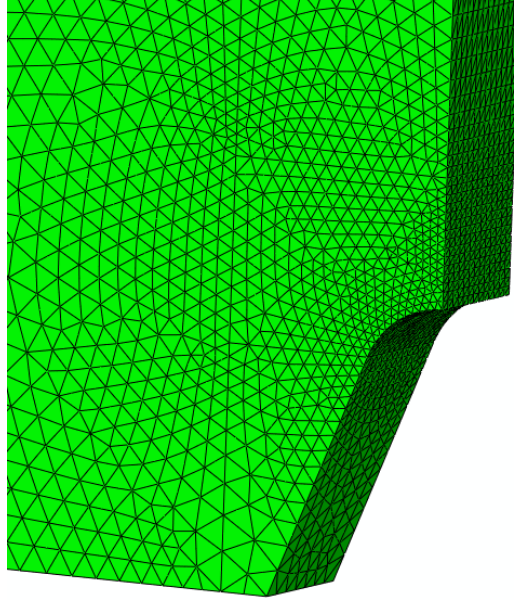


Figure 4.3 Three point bend mesh containing C3D10M (tetrahedral) elements

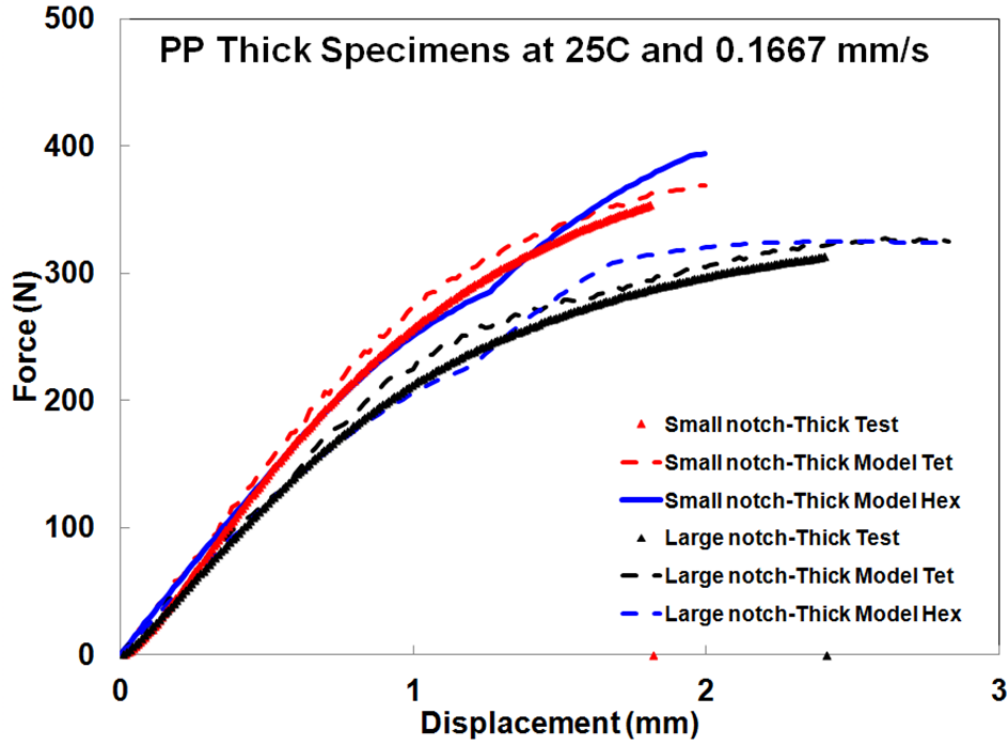


Figure 4.4 Three point bending model results comparing C4D8R (hex) elements and C3D10M (tet) elements

The effects of friction during the impact and three point bending simulations were also investigated. Simulations were initially performed with the contact between the striker and specimen being modeled as frictionless. Other simulations were also performed with friction values of 0.1, 0.5, and 0.9. Figure 4.5 and Figure 4.6 show that for both the impact and three point bend simulations, the frictionless boundary condition produced results that are most similar to the experimental test results. The peak force at failure increased with increasing friction values for impact and three point bend simulations.

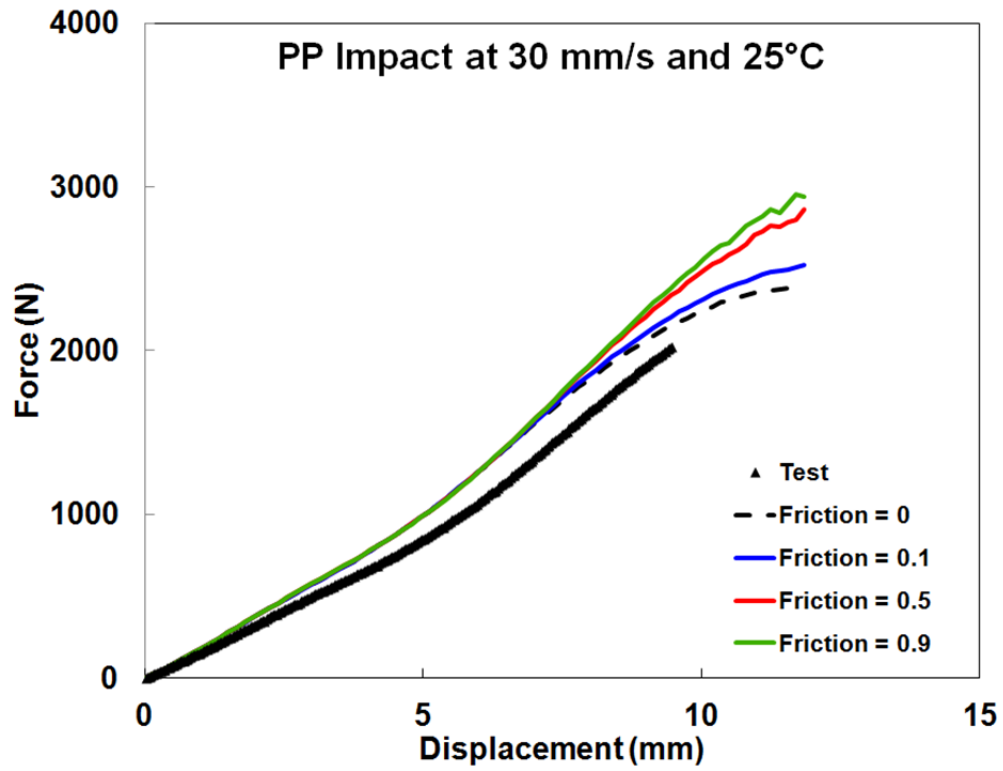


Figure 4.5 Effect of friction during impact simulations of PP at 30 mm/s and 25°C

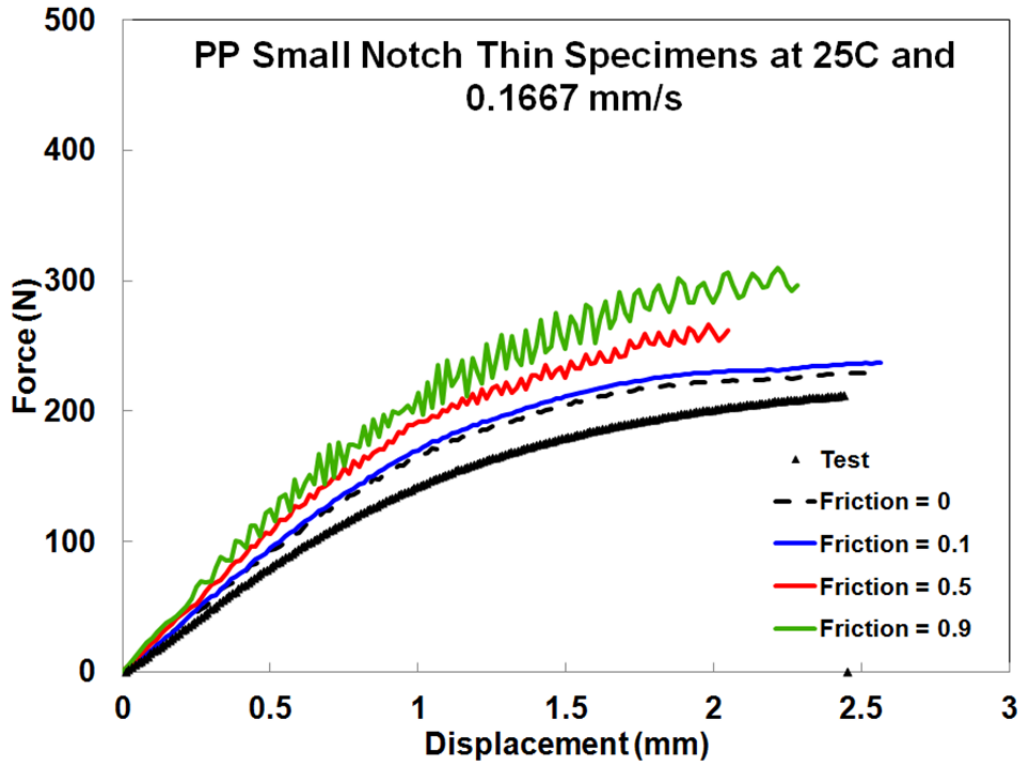


Figure 4.6 Effect of friction during three point bending simulations of PP small notch thin specimens at 0.1667 mm/s and 25°C

### 4.3 Model Results

#### 4.3.1 Compression

A comparison between the experimental data for uniaxial compression and ISV model predictions of PP and co-PP at different temperatures and strain rates is shown in Figure 4.7. The model captures the features of the material response: the elastic regime followed by the nonlinear transition to yield, the yield peak, and the subsequent material softening. The constitutive equations predicted adequately both loading and unloading paths as well as the time and temperature dependence observed in the material response.

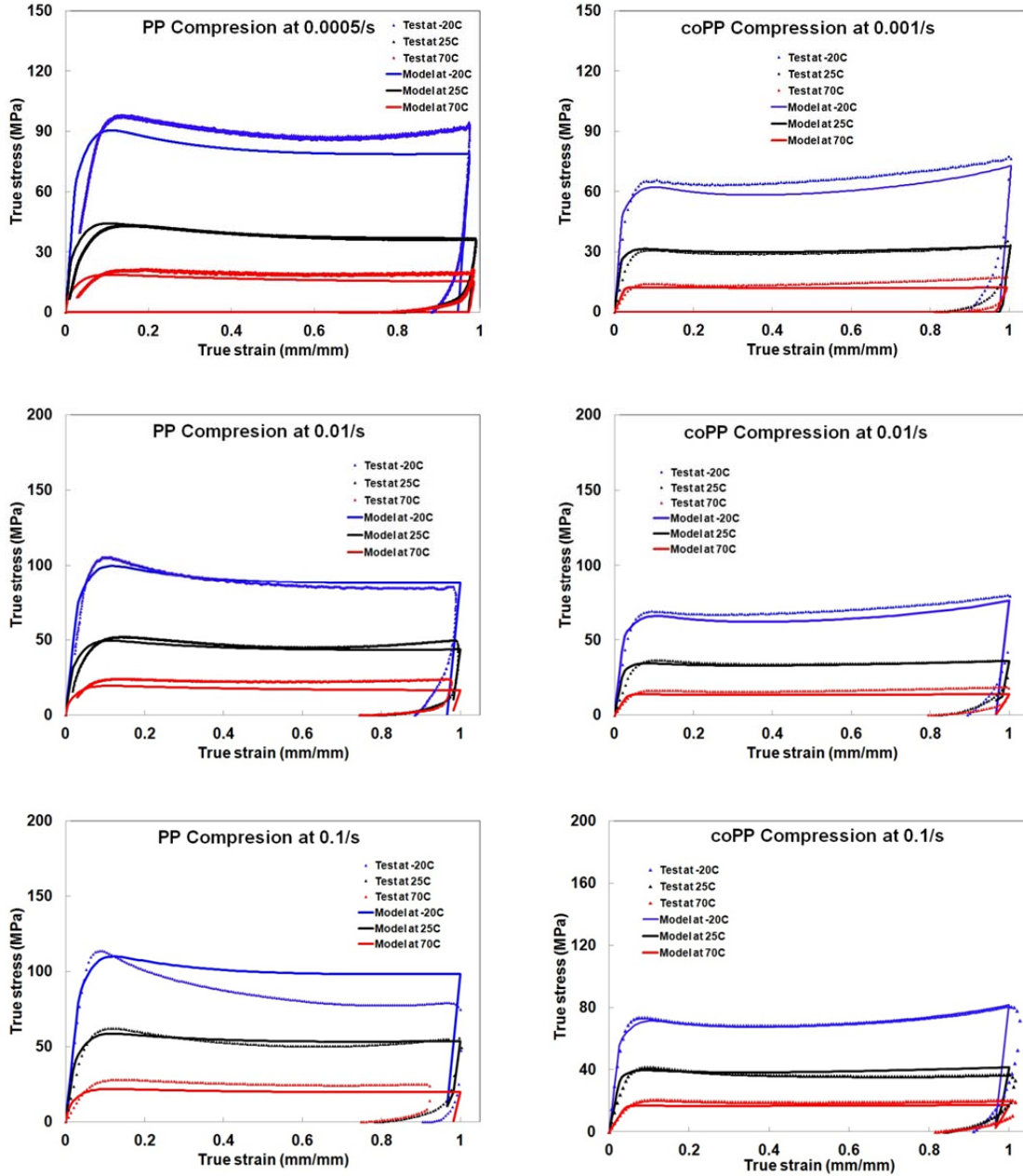


Figure 4.7 Comparison of the ISV based model to the experimental data for uniaxial compression of PP and co-PP at different strain rates and temperatures

#### 4.3.2 Tension

Figure 4.8 displays the prediction of the ISV model on tensile tests of PP at 0.1/s and co-PP at 0.01/s for different temperatures (-20, 25, and 70°C). The numerical

simulation is in good agreement with the test results in terms of yield peak for temperatures of 25°C and 70°C; however, the model over estimates the mechanical response of PP and co-PP at -20°C.

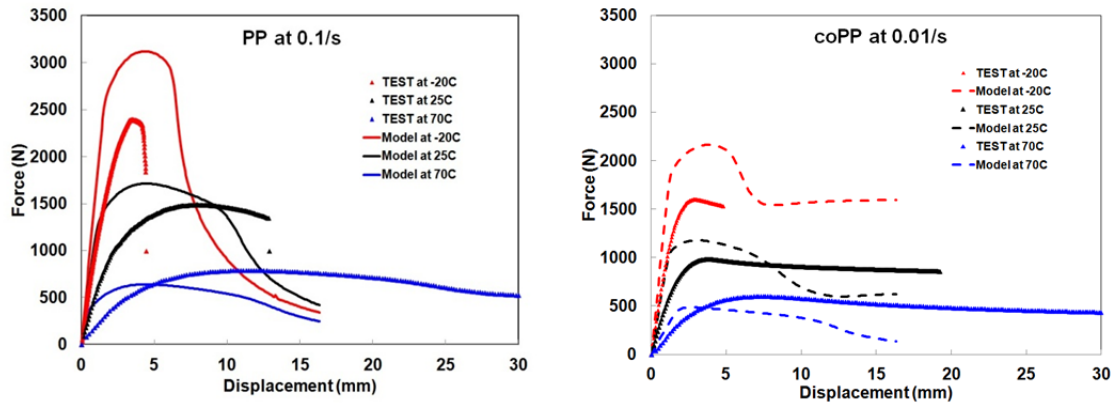


Figure 4.8 Comparison of the ISV model to the experimental data for uniaxial tension of PP at 0.1/s and co-PP at 0.01/s at different temperatures

### 4.3.3 Impact

Figure 4.9 shows a comparison between the ISV model prediction and impact test data for PP and co-PP at velocities of 0.3, 3, and 30 mm/s and at temperatures of -20, 25, and 70°C. The numerical simulations are in good agreement with the test results, reproducing the trend of the force-displacement curves for the different velocities and temperatures. The difference between the test and model may originate from the boundary conditions of the model [23]. Indeed, when conducting the experiment, the plate is claimed to be completely clamped; however, this is very difficult to achieve in reality, so the material plate normally experiences some in-plane displacements around the boundary at a sufficient high load. This can result in slightly lower stiffness values when compared to simulation results in which the plate is modeled as completely



clamped. Another study [24] has shown that the use of lubrication on the striker has a significant effect on the force-displacement curve, especially for ductile materials and large displacements. The higher peak force measured without lubrication is due to more non-localized elastic and plastic bending as well as uniaxial drawing outside the striker hemisphere compared to the more localized biaxial plastic drawing under the striker hemisphere when lubrication is used. However, the lower test results can be explained by damage mechanisms present during testing that the model does not account for.

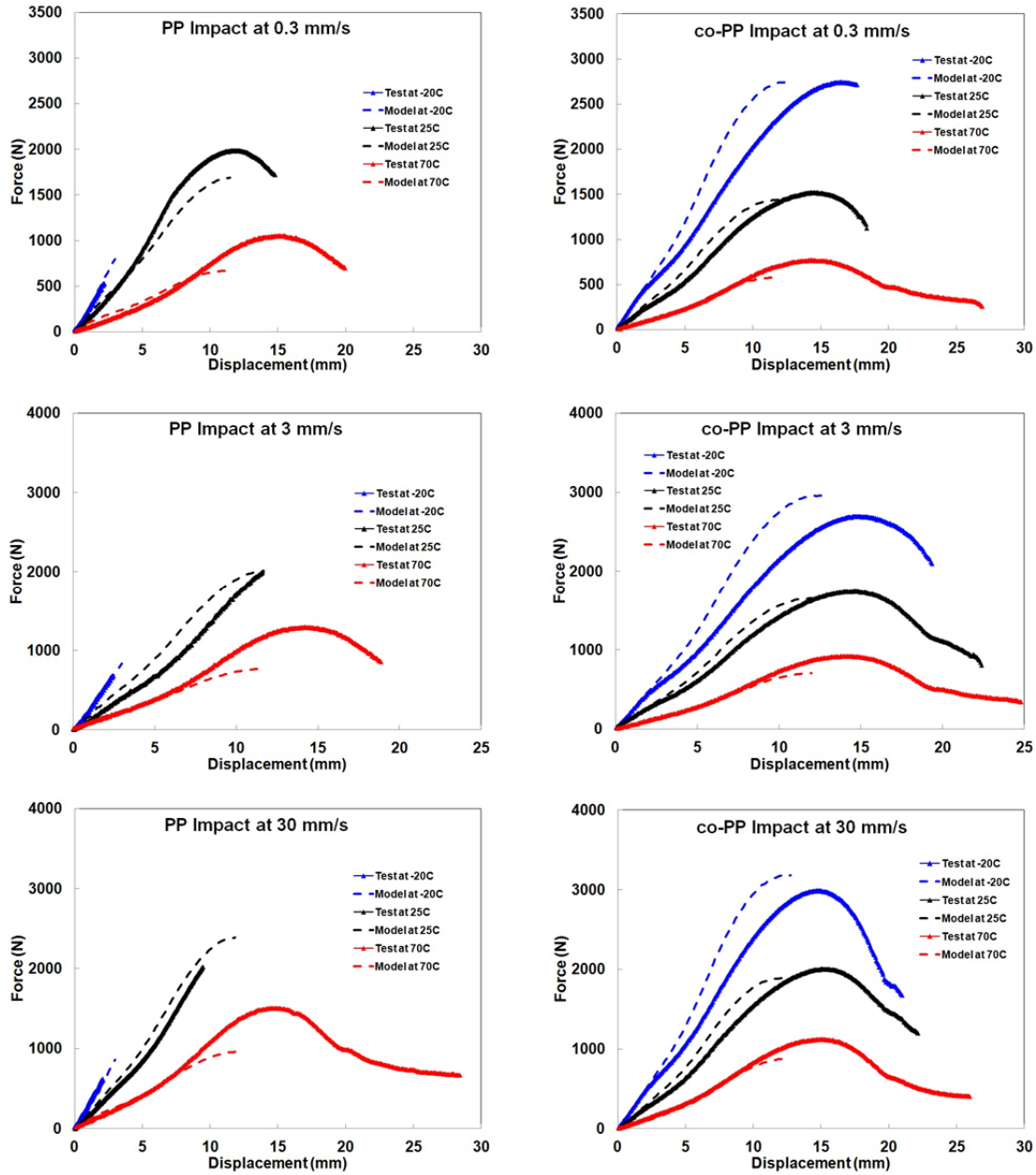


Figure 4.9 Comparison of the ISV model to the experimental data for uniaxial tension of PP at 0.1/s and co-PP at 0.01/s at different temperatures

#### 4.3.4 Three Point Bending

Figure 4.10 shows a comparison between the ISV model prediction and three point bending test data of PP and co-PP for the thin and thick specimens at a velocity of

0.1667 mm/s and temperature of 25°C. The numerical simulations predict with good agreement the maximum stress level observed in the tests before the specimen failure.

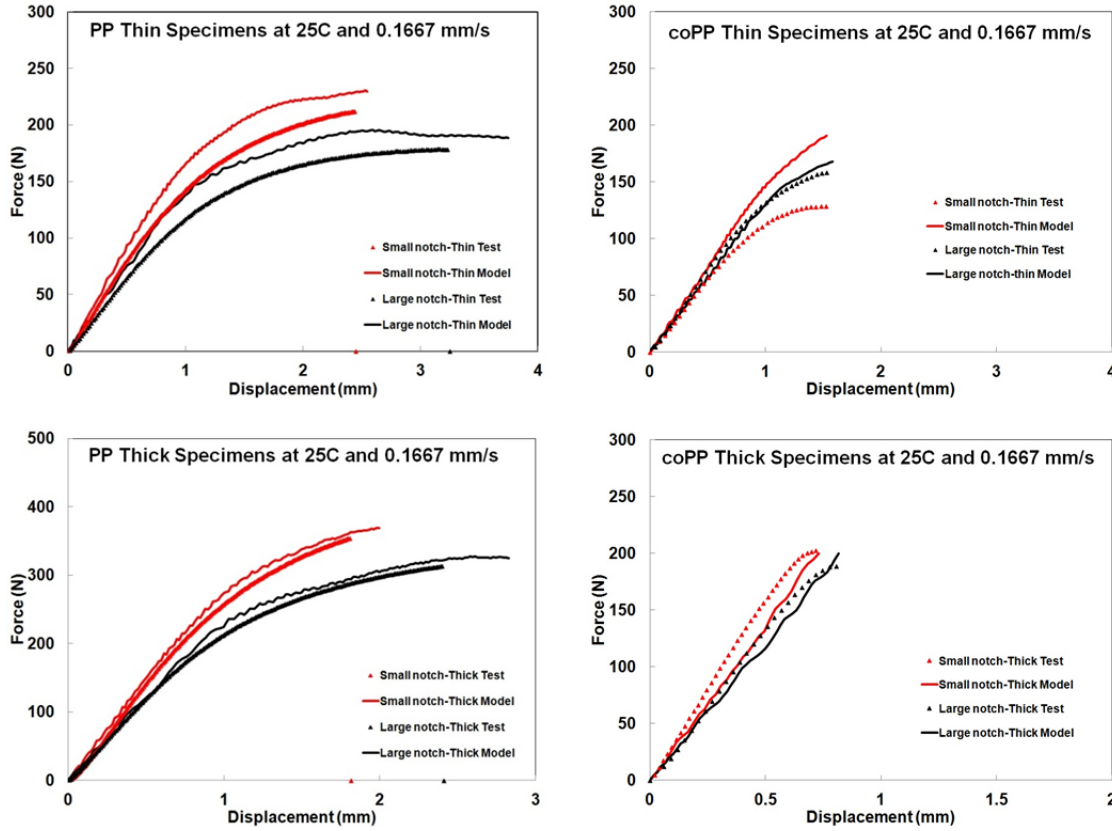


Figure 4.10 Comparison of the ISV model to the experimental data for three point bending of PP and co-PP on thin and thick specimens

To investigate how the stress concentration is influenced by the different geometries of the notch (small vs. large) and specimen thickness (thin vs. thick), the maximum principal stress is plotted on a contour plot of each geometry. Figure 4.11 and Figure 4.12 show the stress concentration at the notch on three point bending tests for PP and co-PP, respectively. By comparing the maximum principal stress at the same exact time during each simulation and by setting the limits of the contour plot equal across all

plots, the influence of the geometry on the stress state can easily be observed. For PP, the small notch thick specimen contained the highest stress concentration while the large notch thin specimen was lowest. Co-PP produces similar results as the PP.

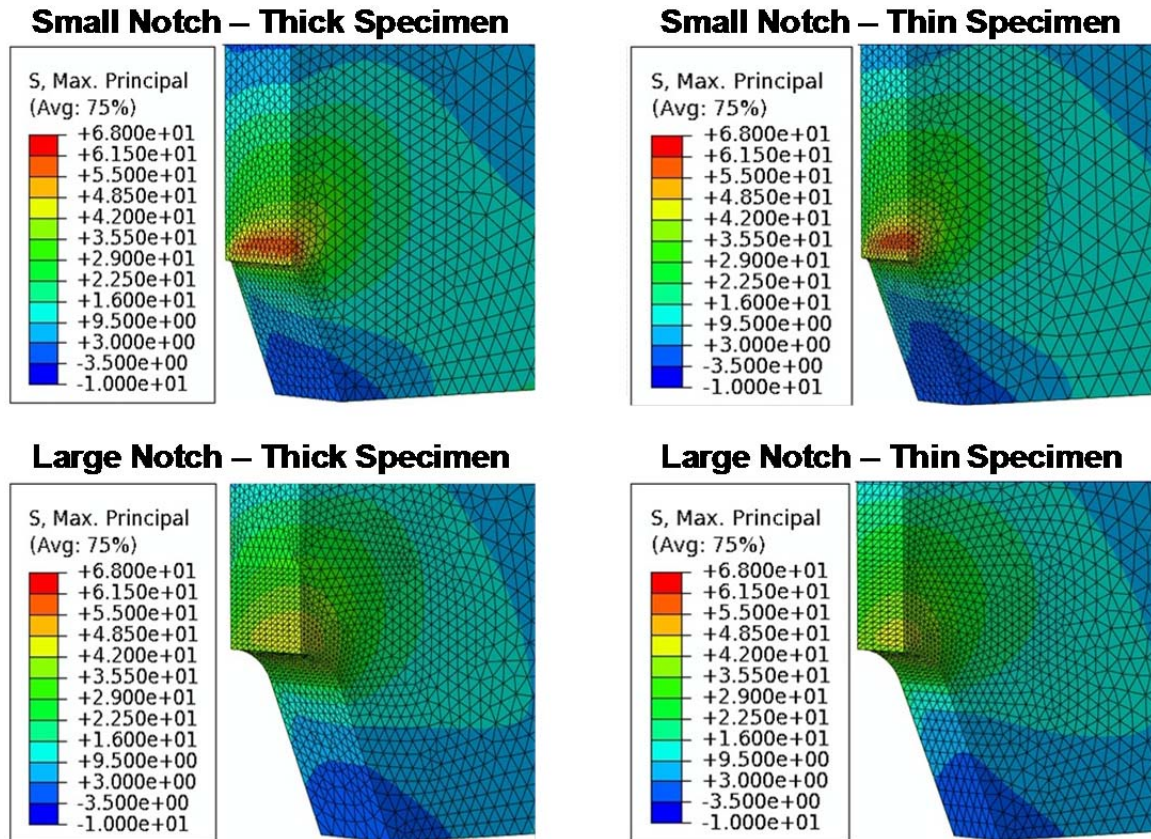


Figure 4.11 Stress concentration at the notch on three point bending tests for PP

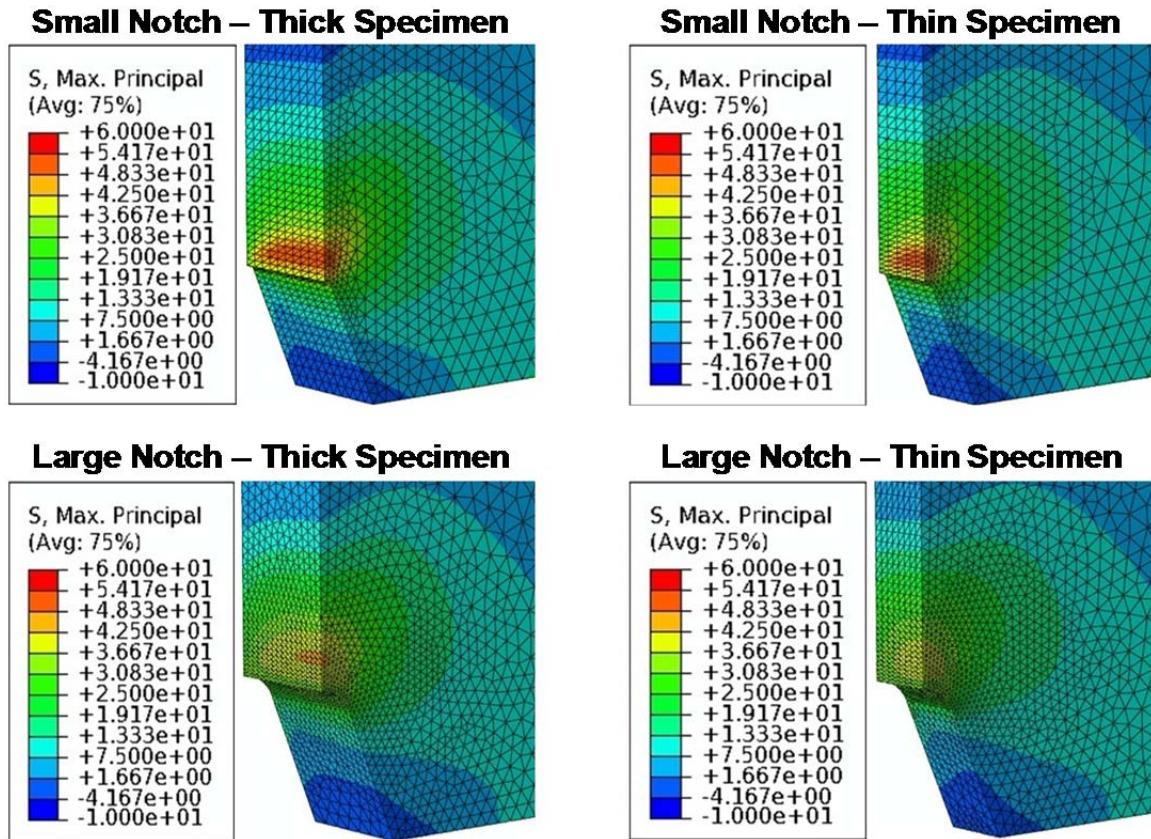


Figure 4.12 Stress concentration at the notch on three point bending tests for co-PP



## CHAPTER V

### APPLICATION OF ACC FAILURE CRITERIA

#### **5.1 Brittle Failure Criteria**

For brittle failure, Woods and Trantina [25] and Woods and Nimmer [26] use a rate dependent maximum principal stress criterion to determine the critical value in which crazes initiate for polycarbonate and polyetherimide. Craze initiation occurs when the maximum principal stress level in a part reaches a critical, rate dependent value. If the maximum principal stress levels stay below those required for craze initiation, then brittle failure will not occur. The critical maximum principal stress as a function of rate is normalized by the rate dependent, yield stress of the material.

The values for maximum principal stress were calculated from the ABAQUS simulations. To retrieve all the necessary data from the simulation results to get the failure criteria, I developed a postprocessor using python script. For each geometry, the maximum principal stress is plotted as a function of displacement as shown in Figure 5.1. The maximum principal stress curves display a plateau which has been marked by a dashed line. After the plateau, several of the curves begin to increase again. This increase is the result of a lack of damage in the model and element distortion as the simulation progresses. This increase is not accounted for in the failure analysis. The maximum principal stress value of the small notch is greater than the maximum principal

stress value of the large notch geometry of corresponding thickness. This is expected since the small notch and thick specimens have a higher stress triaxiality at the notch.

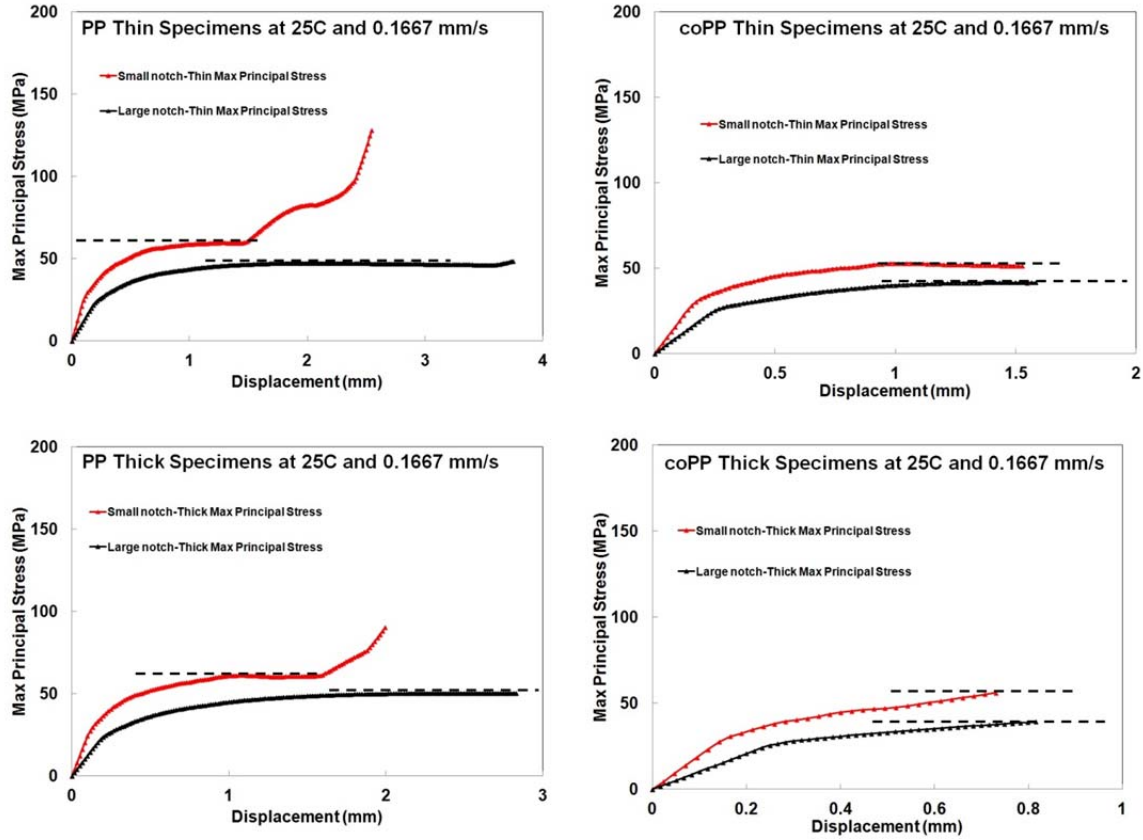


Figure 5.1 Evolution of the maximum principal stress for three point bending regarding the different specimen thicknesses

The stress ratio used by Woods, Trantina, and Nimmer [25-26] is achieved by normalizing the maximum principal stress by the rate dependent yield stress of the material. To calculate this stress ratio, the maximum principal stress obtained from the simulation of the three point bending tests estimated from the plateau of the curve is divided by the yield stress determined from the compression test results. If the stress ratio of a future test is below the stress ratio required for craze initiation, then brittle

failure is not a concern. The procedure to obtain the maximum principal stress failure criterion is outline in Figure 5.2 using PP.

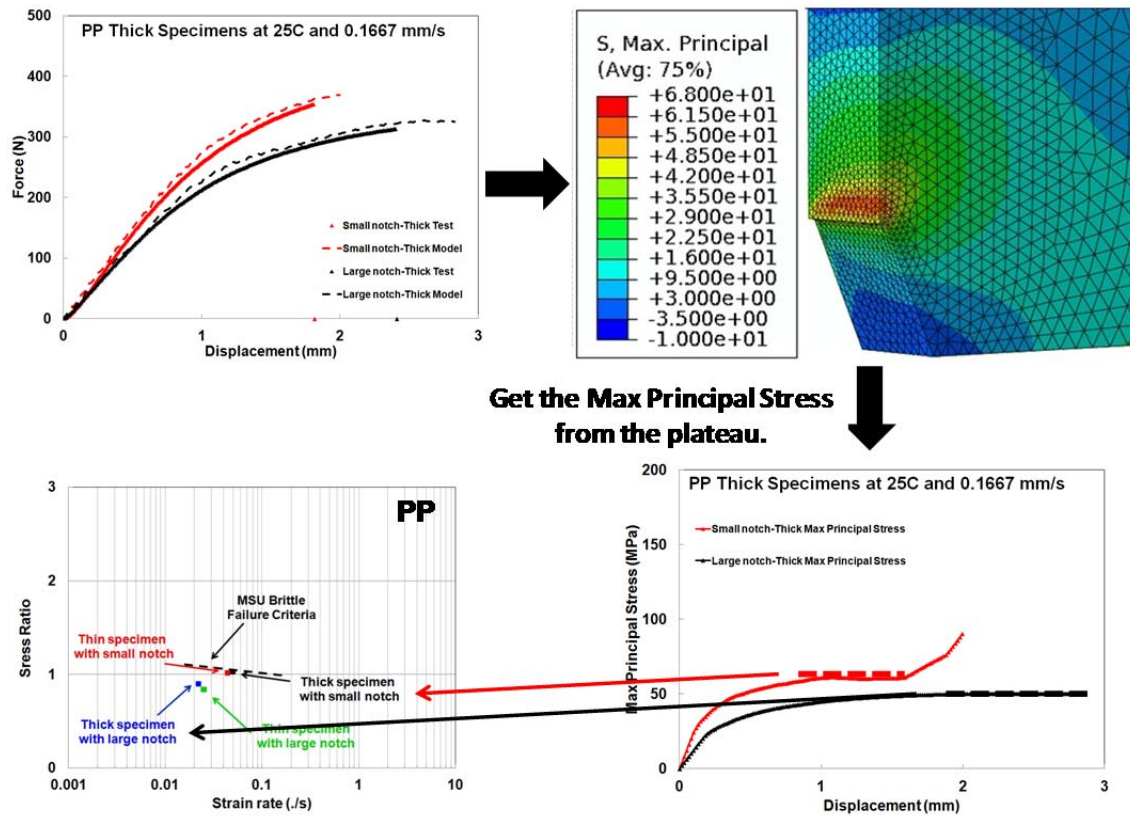


Figure 5.2 Determination of maximum principal stress failure criterion for PP

For verification of this failure criterion, this craze initiation idea is applied to the impact tests to determine if the ductile failure observed during experiments is accurately predicted. The maximum principal stress from the impact simulations at 3mm/s and temperatures of -20, 25, and 70°C are shown in Figure 5.3, and like the three point bending max principal stress curves, a plateau is observed and will be used to estimate the max principal stress. For PP at -20°C, the maximum principal stress is taken at failure since no plateau is present.



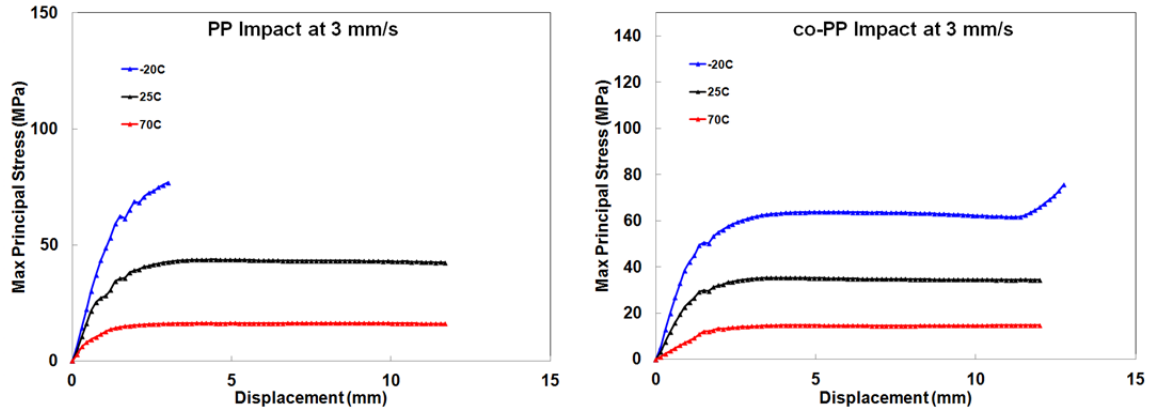


Figure 5.3 Evolution of the maximum principal stress for impact tests at 3 mm/s at -20, 25, and 70°C

Like the three point bending stress ratios, the yield stress is estimated from compression test results at different strain rates and temperatures. The ratio of critical maximum principal stress to yield stress as a function of strain rate for impact tests is plotted in Figure 5.4. For PP, ductile failure for the impact tests is well predicted; however, the brittle failure observed at -20°C is not predicted using this criterion. No co-PP three point bend test experienced brittle failure, so no brittle failure criteria has been established for this material.

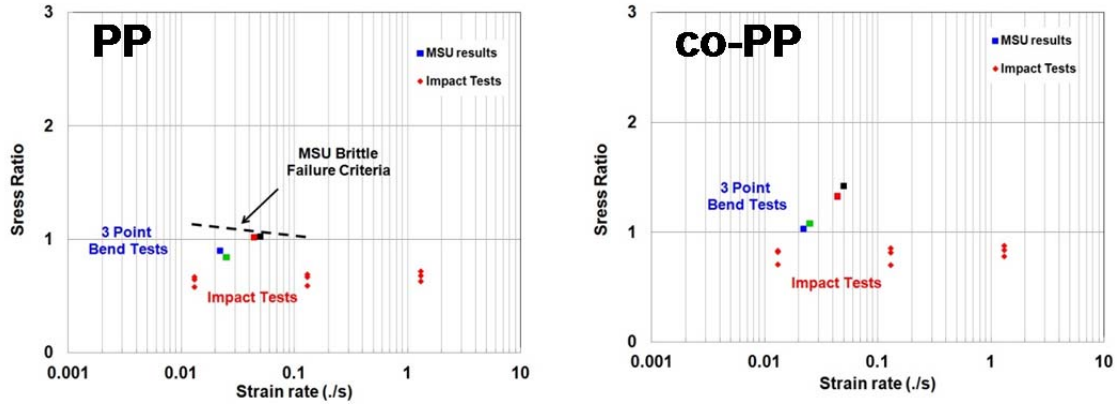


Figure 5.4 Ratio of critical maximum principal stress to yield stress as a function of strain rate for impact tests at different strain rates and temperatures

## 5.2 Ductile Failure Criteria

To determine if ductile failure has occurred in a plastic part, Woods and Trantina [25] suggest a method using equivalent plastic strain levels. Peak equivalent plastic strain levels corresponding to the experimental failure displacements are obtained from finite element predictions and then plotted as a function of the strain rate for each geometry. Equivalent plastic strain values at failure for future tests that are above this line will fail.

Applying the ductile failure criterion to the impact tests, the displacement at the point of maximum loading,  $U_{disp}$ , is determined first. The peak load is chosen for the point of failure since the time when cracks or tears begin to appear is unknown. The equivalent plastic strain at this displacement is then found using results from the simulation. The failure strain as a function of strain rate is then plotted. The preceding process is outline in Figure 5.5. The equivalent plastic strains to failure criteria for PP and co-PP are shown in Figure 5.6. Note that the data for the PP impact tests at  $-20^{\circ}\text{C}$  is omitted from the figure since those tests experienced brittle failure.

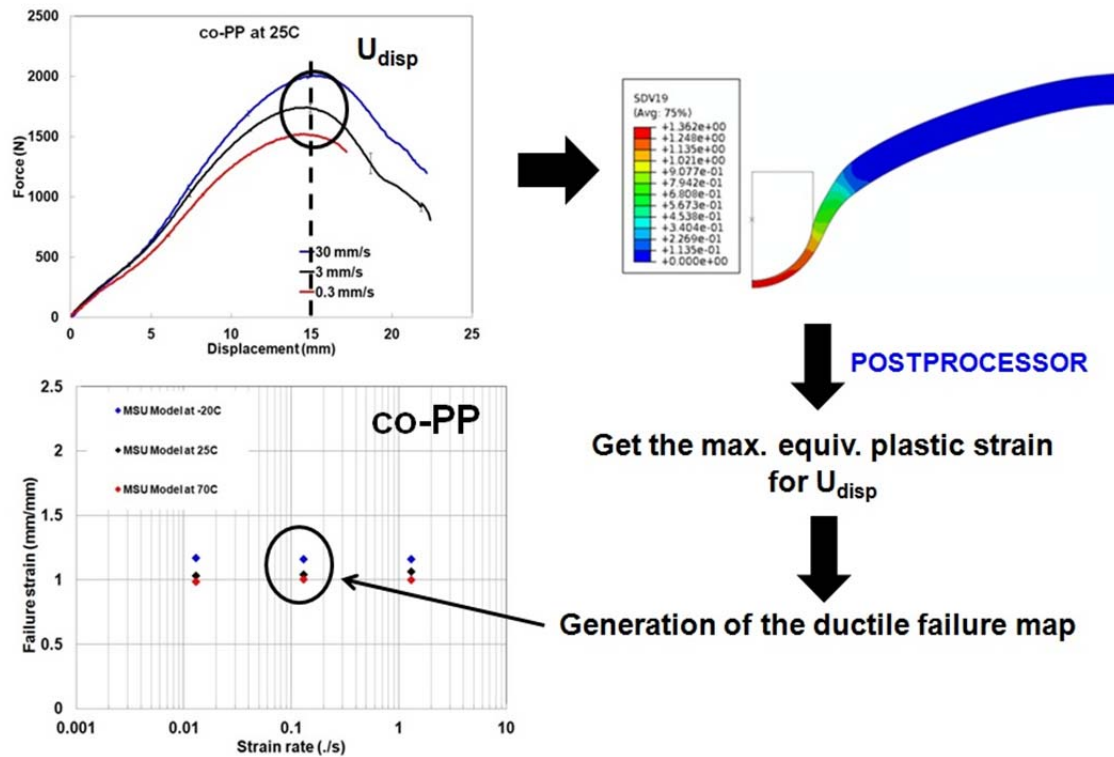


Figure 5.5 Determination of failure strain criterion for co-PP

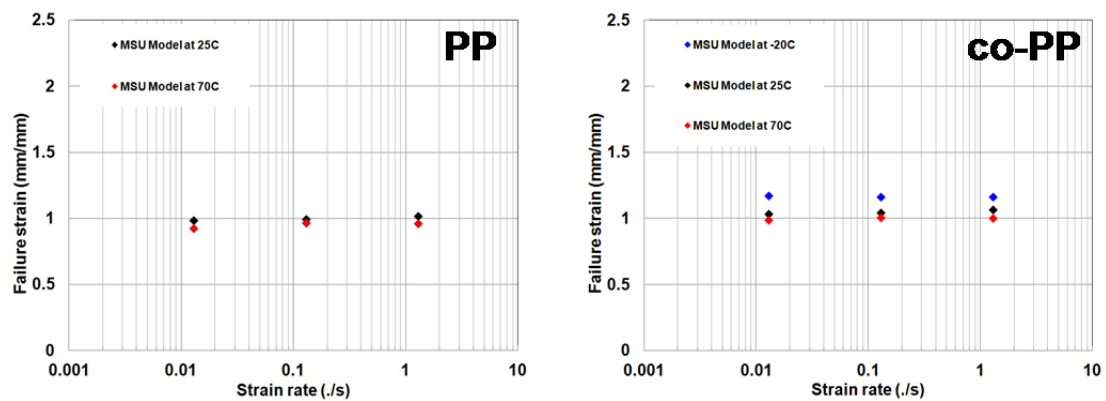


Figure 5.6 Equivalent plastic failure strain as a function of strain rate for impact tests of PP and co-PP at different strain rates and temperatures.

To verify the ductile failure criterion determined from equivalent plastic strain of impact tests, the criterion can also be applied to other test setups. The same criterion has been applied to three point bending tests using the procedure described in Figure 5.5. The equivalent plastic strains of the three point bending tests were obtained from the simulations. Although the criterion does predict ductile failure for some specimens of both PP and co-PP, it is very inaccurate. For instance, Figure 5.7 shows the criteria being applied to co-PP thick specimens with both small and large notches. The maximum equivalent plastic strain for the three point bend tests is much lower than the maximum equivalent plastic strain for the impact, thus no failure is predicted by the ductile failure criteria for these geometries. Experimental testing and an examination of the fracture surfaces show that the co-PP thick geometries did experience ductile failure though.

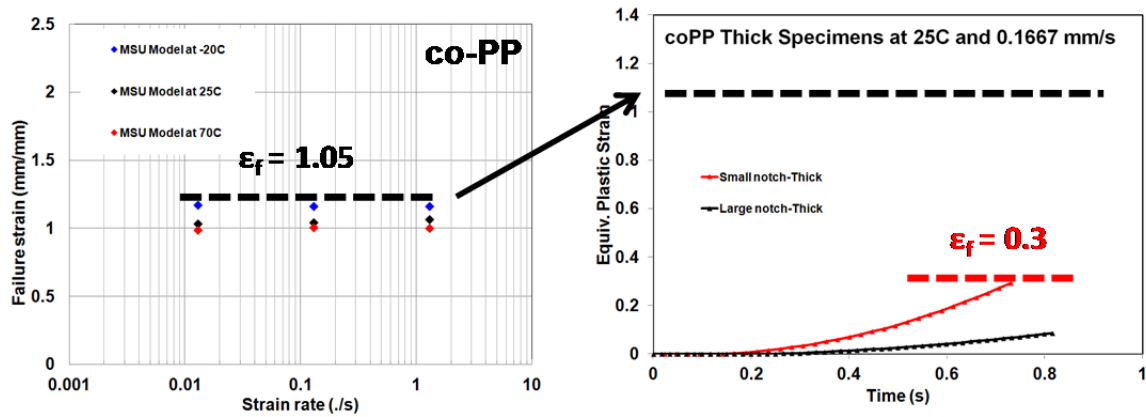


Figure 5.7 Ductile failure criterion applied to three point bending tests for co-PP thick specimens

No failure was predicted when applying the ductile failure criterion to the three point bending simulations, which leads us to the conclusion that the ductile failure criterion needs improving. One possible improvement would be to include a hydrostatic

pressure dependency into the criterion. The material model could also account for the damage mechanisms and material's history in order to more accurately predict material failures.

## CHAPTER VI

### SUMMARY

A testing and modeling methodology has been presented to model the deformation and failure of polypropylene and copolymer polypropylene along with a fractographic study of observed deformation mechanisms. The ISV model integrated into a finite element simulation predicts with good agreement the mechanical behavior of both polypropylene and copolymer polypropylene in compression, tension, impact, and three point bend testing for different strain rates and temperatures, thus capturing the time, temperature, and stress state dependencies of the materials. Two failure criteria have been applied to predict the brittle or ductile failure using the results of the finite element simulations; however, neither criterion has proven effective in its failure predictions.

A sequence of tests was performed to characterize the time, temperature, and stress state dependencies of PP and co-PP to build a material database. In compression, higher rates of loading and lower temperatures lead to higher yield stresses for both materials, yet the yield stress is higher for PP than co-PP in all strain rates and temperatures investigated due to localized plastic deformations due to particles within the co-PP matrix. Co-PP's improved cavitation properties at low temperatures (as compared to PP) that produce more ductile responses are evident from the tension and impact tests performed at -20°C.

The brittle failure criterion based on maximum principal stress was applied to the model to determine the critical value in which crazes initiate. For PP, ductile failure for the impact tests is well predicted when the criterion is calibrated using three point bending tests; however, the brittle failure observed at impact tests of -20°C for PP is not predicted using this maximum principal stress criterion. Also, no co-PP three point bend test experienced brittle failure, so no brittle failure criteria can be established using this method.

The ductile failure criterion based on an equivalent plastic strain was also applied into the model to capture the material failure. Simulations were performed on a three point bending test for a thin, large notch specimen, which exhibits ductile failure. No failure of the specimen was observed while applying the criterion, which leads us to the conclusion that the ductile failure map obtained from impact tests does not predict the ductile failure of three point bending specimens.

Improvements upon both the ISV material model and failure criteria are needed. Many of the predictions overestimate the experimental results. This can be explained by damage mechanisms that are present during testing that the model does not capture. Including damage mechanisms such as crazing, void nucleation, and cavitation into the material model will improve model accuracy. Future work will include the material's history and damage into the material mode.

## REFERENCES

- [1] J. L. Bouvard, D. K. Ward, D. Hossain, E. B. Marin, D. J. Bammann, and M. F. Horstemeyer, "A general inelastic internal state variable model for amorphous glassy polymers," *Acta Mechanica*, vol. 213, no. 1–2, pp. 71–96, Jun. 2010.
- [2] M. F. Horstemeyer, J. Lathrop, a. M. Gokhale, and M. Dighe, "Modeling stress state dependent damage evolution in a cast Al–Si–Mg aluminum alloy," *Theoretical and Applied Fracture Mechanics*, vol. 33, no. 1, pp. 31–47, Feb. 2000.
- [3] Y. Duan, a. Saigal, R. Greif, and M. a. Zimmerman, "Analysis of multiaxial impact behavior of polymers," *Polymer Engineering & Science*, vol. 42, no. 2, pp. 395–402, Feb. 2002.
- [4] M. Ishikawa and I. Narisawa, "Fracture of notched polycarbonate under hydrostatic pressure," *Journal of Materials Science*, vol. 18, no. 7, pp. 1947–1957, 1983.
- [5] M. OYANE, "Criteria of ductile fracture strain," *Bulletin of JSME*, vol. 15, no. 90, pp. 1507–1513, 1972.
- [6] R. Singh, A. Mattoo, and A. Saigal, "Optimizing the design and impact behavior of a polymeric enclosure," *Materials & Design*, vol. 27, no. 10, pp. 955–967, 2006.
- [7] T. Wierzbicki, Y. Bao, Y.-W. Lee, and Y. Bai, "Calibration and evaluation of seven fracture models," *International Journal of Mechanical Sciences*, vol. 47, no. 4–5, pp. 719–743, Apr. 2005.
- [8] M. Zheng, U. Lauschke, and M. Kuna, "A damage mechanics based approach for fracture of metallic components," *Computational Materials Science*, vol. 19, pp. 170–178, 2000.
- [9] S. Sternstein, "Yield criteria for plastic deformation of glassy high polymers in general stress fields," 1969.
- [10] Q. M. Li, "Strain energy density failure criterion," *International Journal of Solids and Structures*, vol. 38, no. 38–39, pp. 6997–7013, Sep. 2001.



- [11] G. Dean and B. Read, "Modelling the behaviour of plastics for design under impact," vol. 20, pp. 677–683, 2001.
- [12] "ExxonMobil <sup>TM</sup> PP1105E1 Datasheet." 2012.
- [13] "ExxonMobil <sup>TM</sup> AXO3BE3 Datasheet." 2012.
- [14] C. Chou, K. Vijayan, D. Kirby, and A. Hiltner, "Ductile-to-brittle transition of rubber-modified polypropylene," *Journal of materials*, vol. 23, pp. 2521–2532, 1988.
- [15] J. Kalfus and J. Jancar, "Morphology of polyolefin surfaces - use of confocal laser scanning microscopy (CLSM)," in "*Polyolefin Composites for Special Purposes*," 2007.
- [16] A. Pawlak and A. Galeski, "Plastic Deformation of Crystalline Polymers: The Role of Cavitation and Crystal Plasticity," *Macromolecules*, vol. 38, no. 23, pp. 9688–9697, Nov. 2005.
- [17] V. Delhay, A. H. Clausen, F. Moussy, O. S. Hopperstad, and R. Othman, "Mechanical response and microstructure investigation of a mineral and rubber modified polypropylene," *Polymer Testing*, vol. 29, no. 7, pp. 793–802, Oct. 2010.
- [18] T. G. Río and J. Rodríguez, "Compression yielding of polypropylenes above glass transition temperature," *European Polymer Journal*, vol. 46, no. 6, pp. 1244–1250, 2010.
- [19] C. Bucknall, "Stress-whitening in high-impact polystyrenes," *Polymer*, vol. 6, 1965.
- [20] R. Gensler, C. J. G. Plummer, C. Grein, and H.-H. Kausch, "Influence of the loading rate on the fracture resistance of isotactic polypropylene and impact modified isotactic polypropylene," *Polymer*, vol. 41, no. 10, pp. 3809–3819, May 2000.
- [21] C. Chou, K. Vijayan, D. Kirby, and A. Hiltner, "Ductile-to-brittle transition of rubber-modified polypropylene," *Journal of materials*, vol. 23, pp. 2533–2545, 1988.
- [22] S. Zebarjad, "Fracture mechanism under dynamic loading of elastomer-modified polypropylene," *Materials Letters*, vol. 57, no. 18, pp. 2733–2741, May 2003.
- [23] M. Polanco-Loria, A. Clausen, and T. Berstad, "Constitutive model for thermoplastics with structural applications," *International Journal of*, vol. 37, no. 12, pp. 1207–1219, 2010.

- [24] H. Daiyan, E. Andreassen, F. Grytten, O. V. Lyngstad, T. Luksepp, and H. Osnes, “Low-velocity impact response of injection-moulded polypropylene plates – Part 1 □: Effects of plate thickness , impact velocity and temperature,” *Polymer Testing*, vol. 29, no. 6, pp. 648–657, 2010.
- [25] J. Woods and G. Trantina, “Material Characterization for Predicting Impact Performance of Plastic Parts,” *SAE Technical paper*, 1999.
- [26] J. Woods and R. Nimmer, “Design aids for preventing brittle failure in polycarbonate and polyetherimide,” in *Failure Analysis and Prevention. Plastics Design*, 2001, pp. 267–274.

APPENDIX A

INTERNAL STATE VARIABLE MODEL CALIBRATION

## A.1 One Dimensional Model

The one dimensional model is used to fit the model parameters at different strain rates and temperatures regarding uniaxial loading conditions. Table A.1 gives a summary of the equations used in the one dimensional model.

Table A.1 One dimensional model summary

<p><b><u>Cauchy Stress</u></b></p> <p>➤ <math>\boldsymbol{\sigma} = \boldsymbol{\tau} = \overline{\mathbf{M}}</math></p> <p><math>\overline{\mathbf{M}} = 2\mu(\theta)\ln\lambda^e \mathbf{D}</math></p> <p><math>\mu(\theta) = \frac{E(\theta)}{(2 + 2\nu)}, K(\theta) = \frac{2\mu(\theta)(1 + \nu)}{3(1 - 2\nu)}</math></p> <p><math>E(\theta) = (E_{ref} + E_1(\theta - \theta_{ref})) \left( 1 + \frac{a}{1 + e^{\frac{\log(\dot{\epsilon}) - \log(\dot{\epsilon}_{ref})}{b}}} \right)</math></p>
<p><b><u>Internal State Variables</u></b></p> <p>➤ <math>\bar{\kappa}_1 = c_{\kappa_1}(\theta)\bar{\xi}_1; c_{\kappa_1}(\theta) = \alpha_1\mu(\theta)</math></p> <p><math>\dot{\bar{\xi}}_1 = h_0 \left( 1 - \frac{\bar{\xi}_1}{\bar{\xi}_1^*} \right) \dot{\gamma}^p</math> with <math>\bar{\xi}_1^* = (\bar{\xi}_{sat}^*(\theta) - g_0(\theta)\bar{\xi}_1^*) \dot{\gamma}^p</math></p> <p><math>g_0(\theta) = C_9(\theta - \theta_{ref}) + C_{10}</math> and <math>\bar{\xi}_0^*(\theta) = C_5(\theta - \theta_{ref}) + C_6</math></p> <p><math>\bar{\xi}_{sat}^*(\theta) = C_7(\theta - \theta_{ref}) + C_8</math></p> <p>➤ <math>\bar{\kappa}_2 = c_{\kappa_2}(\theta)\bar{\xi}_2; c_{\kappa_2}(\theta) = \alpha_2\mu(\theta)</math></p> <p><math>\dot{\bar{\xi}}_2 = h_1(\bar{\lambda}^p - 1) \left( 1 - \frac{\bar{\xi}_2}{\bar{\xi}_{2sat}(\theta)} \right) \dot{\gamma}^p;</math></p>

Table A.1 (Continued)

<u>Flow rule</u>
$\triangleright \quad \dot{\mathbf{F}}^p \mathbf{F}^{p-1} = \bar{\mathbf{D}}^p = \frac{\dot{\lambda}^p}{\lambda^p} \mathbf{D}; \quad \bar{\mathbf{D}}^p = \frac{1}{\sqrt{3}} \dot{\gamma}^p \text{sign}(\text{dev}(\bar{\mathbf{M}} - \bar{\boldsymbol{\alpha}})) \mathbf{D}$
$\dot{\gamma}^p = \dot{\gamma}_0^p e^{\left[ \frac{-\Delta H_\beta}{R\theta} \right]} \left[ \sinh \left( \frac{\bar{\tau}_{\text{eq}} V}{2k_B \theta} \right) \right]^m$
$\bar{\tau} = \frac{\sqrt{3}}{2}  \text{dev}(\bar{\mathbf{M}} - \bar{\boldsymbol{\alpha}}) ; \quad \bar{\tau}_{\text{eq}} = \bar{\tau} - (Y(\theta) + \bar{\kappa}_1 + \bar{\kappa}_2 + \alpha_p \bar{\pi})$
$Y(\theta) = C_3 (\theta - \theta_{\text{ref}}) + C_4$

## A.2 Parameters Identification

The one dimensional equations have been implemented in MATLAB using three main functions: lsqnonlin, ode15s, and interp1. The function lsqnonlin is used for the minimization of the least squares expression using the trust region method in combination with the Newton method. The function ode15s is a multistep solver for one-dimensional evolution equations (ODEs) that integrates the nonlinear ODEs for the state variables of the model. The last function, interp1, interpolates the computed response to obtain the stress level at the corresponding experimental strain value. The model is calibrated using the following steps:

First, the model is calibrated for  $T = T_{\text{ref}}$  following the steps described below:

- 1) **Elastic regime** ( $\{E_1, a, b, \dot{\epsilon}_{\text{ref}}, \nu\}$ ): the elastic modulus is identified from mechanical tests. The set of parameters  $\{a, b, \dot{\epsilon}_{\text{ref}}\}$  is fitted on the elastic

modulus at different strain rates. The elastic bulk modulus is estimated from  $K = 2\mu (1+\nu) / (3(1-2\nu))$ , where  $\nu$  is the Poisson's ratio, a value typically available in the literature.

- 2) **Time dependence** ( $\{\dot{\gamma}_0^p, \Delta H_\beta, V, m, C_4\}$ ): This set of parameters is fitted to capture the time dependence of the material as depicted in Figure A.1 (a).
- 3) **Strain hardening** ( $\{C_2, \lambda_L, C_{14}\}$ ): the strain hardening at large strain level is fitted using this set of parameters as depicted in Figure A.1(b).
- 4) **Strain softening** ( $\{C_6, C_8, \bar{\xi}_{10}, h_0, C_{10}, C_{\kappa_1}\}$ ): these parameters are fitted in order to capture the nonlinear yield peak. The parameter  $\{\bar{\xi}_{10}\}$  is assumed to be fixed as  $\bar{\xi}_{10} = 0$ . The stress amplitude is fitted using  $\{C_{\kappa_1}, \bar{\xi}_0^*\}$ . Then,  $\{\bar{\xi}_{sat}^*, h_0, g_0\}$  are fitted to capture the nonlinear yield peak as observed in Figure A.1(c).
- 5) **Identification of**  $\{h_1, C_{12}, C_{\kappa_2}\}$ : this set of parameters captures the Bauschinger effect observed during the unloading path (Figure A.1(d)).
- 6) **Identification of**  $\alpha_p$ : The value of the pressure sensitivity parameter is chosen from the literature or can be fitted on tensile tests in order to capture the correct yield stress amplitude.

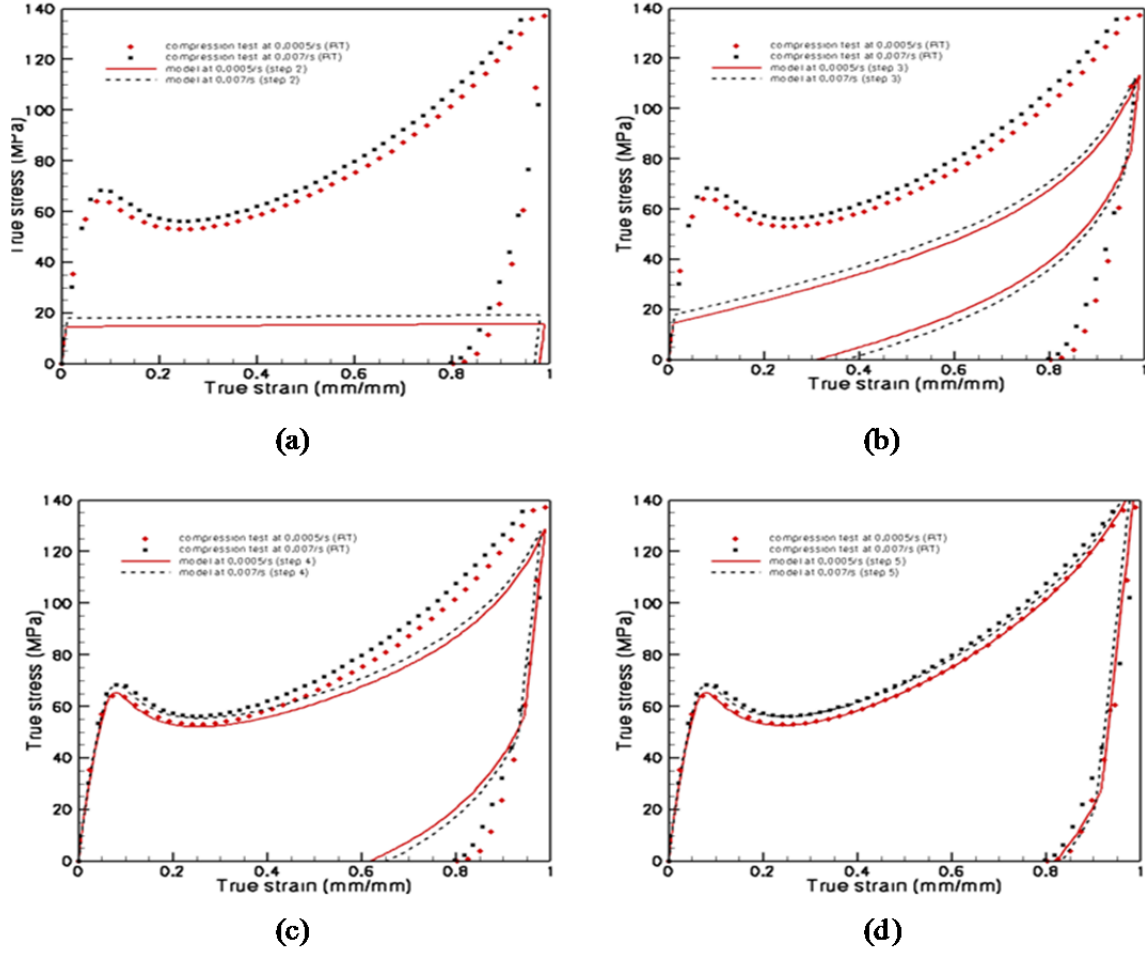


Figure A.1 Description of the different steps to fit the material parameters: (a) capturing the time dependence, (b) capturing the strain hardening, (c) capturing the nonlinear yield peak, and (d) capturing the unloading of the Bauschinger effect.

The model is then calibrated for different temperatures following the steps described below:

- 7) **Elastic regime** ( $\{E_{ref}\}$ ): the elastic modulus is identified from mechanical tests.
- 8) **Time dependence** ( $\{C_3\}$ ): This parameter is fitted to capture the time dependence of the material.

- 9) **Strain hardening** ( $\{C_1, \lambda_L, C_{13}\}$ ): the strain hardening at large strain level is fitted using this set of parameters.
- 10) **Strain softening** ( $\{C_5, C_7, C_9\}$ ): these parameters are fitted in order to capture the nonlinear yield peak.
- 11) **Identification of**  $\{C_{11}\}$ : this parameter captures the Bauschinger effect observed during the unloading path.



## APPENDIX B

### GEOMETRY AND BOUNDARY CONDITIONS OF NUMERICAL SIMULATIONS

## B.1 Tensile Simulations

The geometry, dimensions, and boundary conditions of the problem are presented in Figure B.1. The inhomogeneous tensile response of necking is initiated by including a small geometrical defect in the specimen. This defect was introduced by decreasing the length  $W_d$  with  $W_d = \alpha W_0$  and  $\alpha = 0.98$  (corresponding to the ASTM638-03 tolerance permitted for specimen width). Due to the symmetries of the problem, a quarter of the specimen is modeled with symmetry boundary conditions. The mesh is composed of 8-nodes reduced integration elements

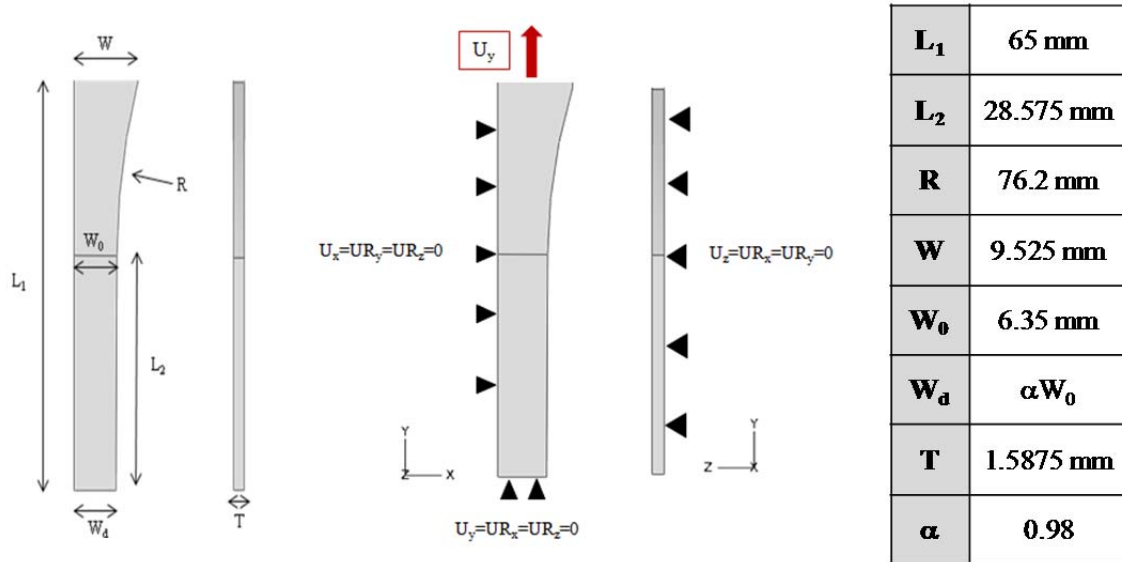


Figure B.1 Geometry, dimensions, and boundary conditions for tension simulations

## B.2 Impact Simulations

Taking into account the symmetries of the problem, an axially symmetric analysis is considered. Figure B.2 shows the geometry of the model and its boundary conditions.

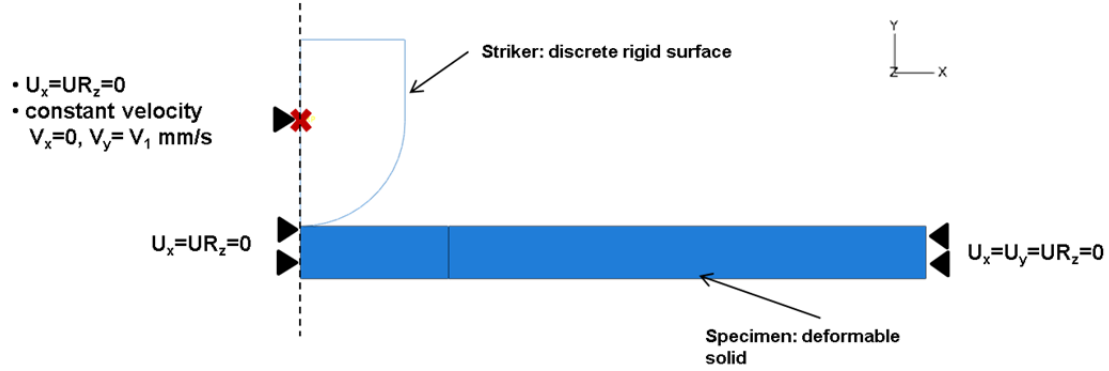


Figure B.2 Boundary conditions for axisymmetric impact simulations

A surface-to-surface contact is used to take into account the contact of the striker with the specimen. The geometries of the surfaces in contact are shown in Figure B.3.

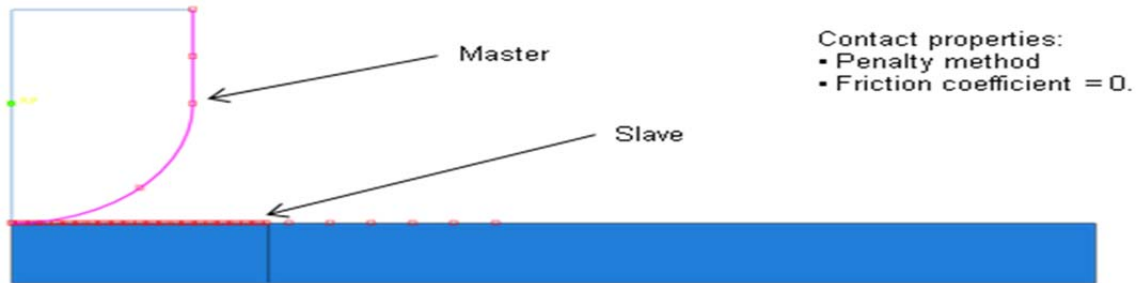


Figure B.3 Surface to surface contact used during impact simulations

As the striker is a rigid surface and meshed with coarse elements, it was chosen to be the master surface. This surface is defined using the rigid elements of the striker and described by its normal that is oriented toward the slave surface. The contact algorithm uses a penalty method. The friction is neglected in these simulations.

The mesh of the system is shown by Figure B.4. The specimen was meshed using CAX4R elements. The impact zone has a mesh size of 0.1 mm, and the rest of the specimen has a size of 1.45 mm. An adaptive mesh domain is defined in the area that is

or will be in contact with the striker. The adaptivity of the mesh ensures that large deformations will be accepted by the mesh throughout the analysis. With this feature, the computation is able to complete, even if it is a costly method in term of computational time. The striker was meshed using RAX2 elements.

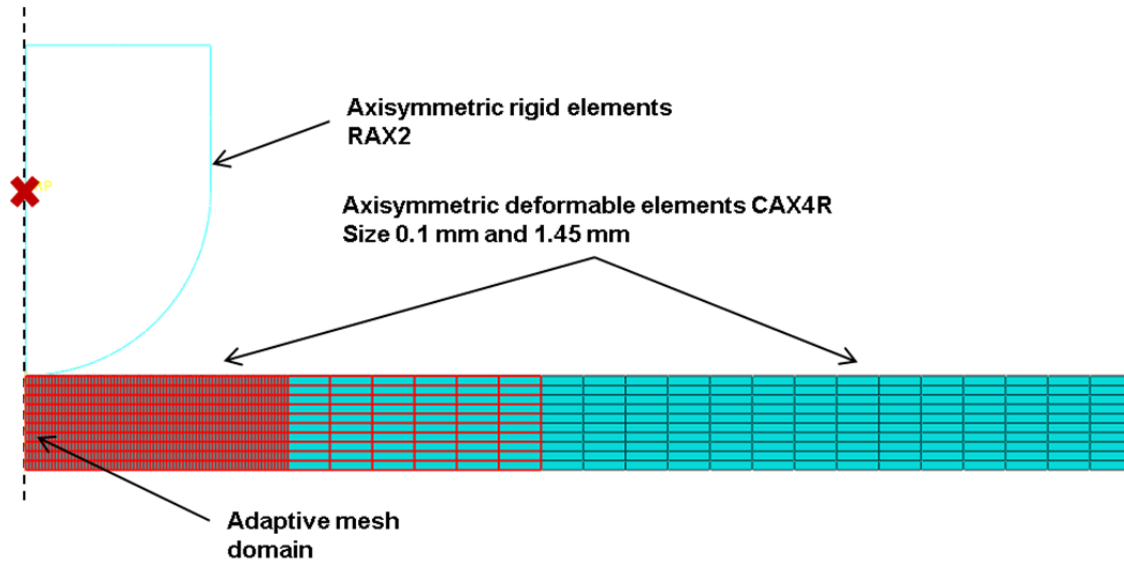


Figure B.4 Mesh of impact specimens used for simulations

### B.3 Three Point Bending Simulations

The geometry, boundary conditions and loading used for the three-point bending simulation are presented in this section. Only a quarter of the specimen is modeled with symmetry boundary conditions because of the symmetry of the problem. Figure B.5 shows the dimensions of the specimen and the boundary conditions due to the symmetries. The black triangles indicate the symmetry boundary conditions in the x and z directions, and the downward arrow shows where the load is being applied to the top roller. The roller under the specimen has zero degrees of freedom.

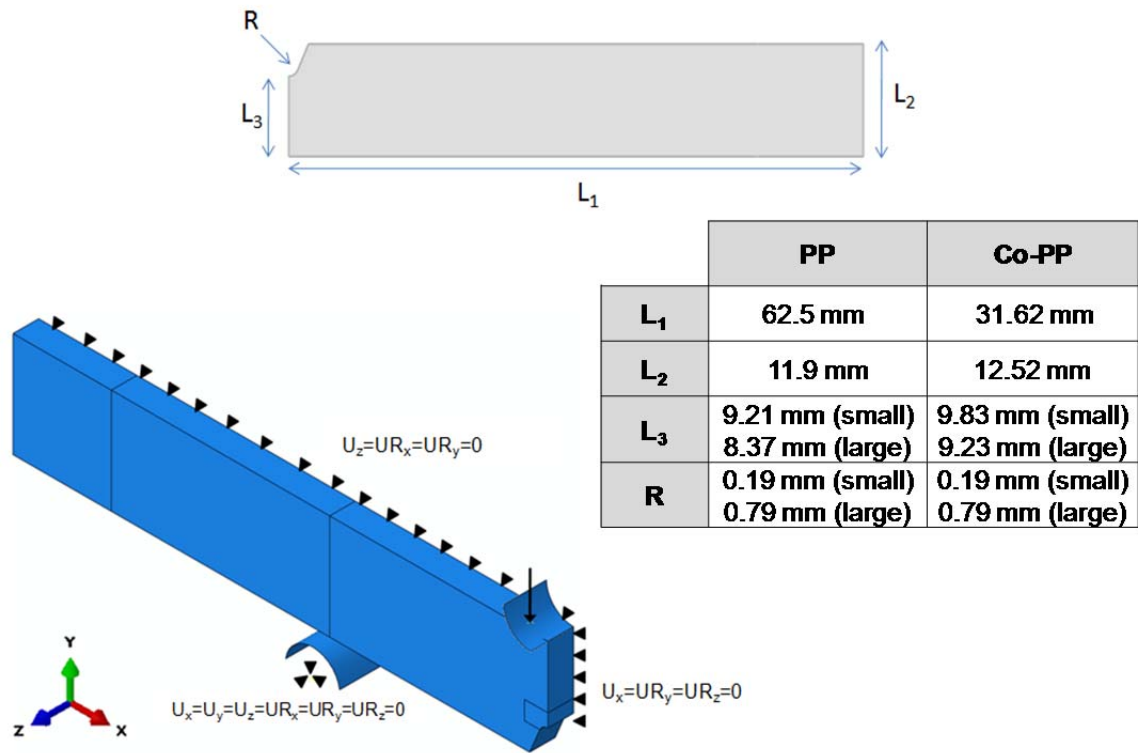


Figure B.5 Dimensions and boundary conditions of the three point bend model